Part II

Collisions Between Disks

6

Elliptical galaxies from mergers of disks *

Abstract
We have carried out a number of N-body experiments involving encounters between disk galaxies. Two sets of experiments are presented. The first one involves galaxies with a disk, bulge and halo (dbh models). The second one involves encounters between galaxies with disk and halo (dh models). The initial realizations are placed on inter-penetrating elliptical orbits leading to merger. The remnants of 18 merger experiments are fully analyzed. A morphological description and photometric and kinematic observables are given for the remnants. The results are compared in order to see a possible difference between the absence and presence of a bulge. Our dbh experiments include more massive bulges than found in similar works published in the literature. Some important differences arise from this distinction, and our results are compared with observations. The simulations provide support for the hierarchical merging scenario for the formation of ellipticals.

1 Introduction

Toomre & Toomre (1972) and Toomre (1977) put forward the merger hypothesis for the formation of elliptical galaxies. In their view, elliptical galaxies may form via collisionless mergers of disk galaxies. Observations of merging galaxies support this idea, as do some characteristics of elliptical galaxies such as shells, ripples, kinematically distinct cores, misaligned rotation axes and disky-boxy isophotal shapes (see Schweizer 1998 for a review).

Barnes (1988, 1992) further developed this idea by carrying out N-body simulations of mergers invoquing equal-mass model galaxies composed of a non-rotating bulge, a disk and a dark matter halo. He concluded that the remnants of his experiments are quite similar to real-life elliptical galaxies.

The most complete study to date on the characteristics of remnants of disk galaxies is the series of papers by Hernquist and collaborators (1992, 1993; Hernquist et al. 1993; Heyl et al. 1994, 1995, 1996). The authors explore the outcome of mergers of both bulgeless systems and systems a with bulge, and compare them to each other and to real elliptical

*Antonio César González-García & Marc Balcells

galaxies. They conclude that bulgeless systems are not likely the progenitors of today's elliptical galaxies due to the low density in the inner regions of disks. This difficulty was first put forward by Ostriker (1980) in a short but famous paper. The solutions proposed to overcome this problem are two fold: the introduction of gas, or a third component, i.e. a bulge. Subsequently, Hernquist et al. explored what the effect of introducing a bulge is. They find that the presence of bulges may be a viable solution, since the density problem is solved. Their models can explain many properties of elliptical galaxies.

Barnes (1998) further explored the merging hypothesis by simulating mergers of disks with a mass ratio of 3:1. From comparing these systems with 1:1 merger remnants he finds some differences. Properties of remnants from 1:1 mergers strongly depend on the initial orbital geometry. However 3:1 mergers do not show this dependency and furthermore seem more likely to form systems that resemble S0 galaxies.

Balcells & González (1998) studied a number of merger remnants from collisions with mass ratio 1:1, 2:1 and 3:1 with an orbital configuration chosen such as to produce counter rotating cores in the final elliptical and S0 galaxies. They found that collisionless spiral-spiral mergers may result in elliptical remnants with counter-rotating cores without the recourse to gas dynamics proposed by Hernquist & Barnes (1991).

Naab et al (1999) explored 1:1 and 3:1 mass-ratio mergers. They found that 1:1 remnants are likely related to ellipticals with a boxy deviation from elliptical isophotes, while 3:1 form disky objects instead. They also concluded there is no need to introduce gas in order to explain disky isophotes in elliptical galaxies.

Bendo & Barnes (2000) studied the remnants of merger simulations with mass ratios 1:1 and 3:1 with various initial geometrical configurations. They aimed to find what kinematic structures can be observed that are comparable to real E's. They found that they can explain many characteristics, like misaligned rotation, counter-rotation and rapid rotation.

However Cretton et al. (2001) and Naab et al. (2001) disagree with Bendo & Barnes in a number of kinematic diagnostics. Both studied mergers with mass ratio 1:1 and 3:1. Cretton et al. found that the rotation is too low when compared with the elliptical galaxies in the sample of Rix et al. (1999), although Bendo & Barnes performed the same comparison and found no disagreement. Naab et al. (2001) studied the line-of-sight velocity distribution of mergers of 1:1 and 3:1 mass ratio to see if the disky ones follow the same trend of v/σ with the third moment, h_3, as observed by Bender et al. (1994). They observed that their merger remnants do not follow this trend. To do so they needed to introduce a disk with at least 10 to 20% of the mass. They proposed gas as the means to produce this disk.

2 Motivation

In the chapters devoted to E-E mergers it has been shown that mergers of systems which initially lie on the Fundamental Plane relation (FP hereafter) generate systems that also lie on the FP relation, and we concluded that mergers of ellipticals on the FP do not destroy the FP.

We now wish to study whether this FP relation can be created via purely stellar (collisionless) mergers of spiral galaxies. Hints on this way of thinking are given by the work of Capelato et al. (1995). Their initial systems are King models with soft cores ($\log r_t/r_c = 1.03$). These profiles are closer to those of globular clusters than to those of elliptical galaxies, and therefore initially they would be outside the FP. At the end of their simulations the elliptical that is formed via a merger lies on the FP. In this sense we want to see if via collisionless

mergers of spirals, that are also outside the FP, the remnant would lie on the FP.

Barnes (1988, 1992, 1998 and references therein), Hernquist (1992,1993), and Barnes & Hernquist (1992) studied the final structure and dynamics of a series of different merger experiments. In those papers they provide a wealth of information on phenomenological results as well as on the dynamics of how the merging process reorganizes the mass distribution of the intervening galaxies. However they do not discuss the position of their merger remnants with respect to the FP.

Hernquist et al. (1993), while studying the phase-space density for merger remnants, propose a correlation between the central phase-space density and luminosity.They find that this correlation can be interpreted as arising from the growth of elliptical galaxies via mergers.

Bekki (1998) carried out a number of experiments concerning the FP resulting from mergers of star-forming, gas-rich disks. In those runs the remnants lie close to the FP. Bekki argues that gas plays a key role in achieving this result, through the transformation of a great deal of gas into stars and in this way creating the FP.

To study whether the role of gas and star formation is essential in creating the FP, we have carried out experiments aimed at investigating whether the FP can be created from collisionless mergers of disk galaxies. Two sets of experiments are considered. In the first we use systems with disk, bulge and halo (referred to as dbh from now on). In the second we use systems with disk and halo (dh from now on).

In merger models of dbh systems we have already a part of the luminous system, namely the bulge, with characteristics similar to those of an elliptical galaxy. So we want to see how not having a bulge can affect the final merger model and whether or not it will lie on the FP.

We have chosen our disk galaxies to follow a Tully-Fisher type relation for the different mass ratios. To do so we have developed a scaling law from this empirical relation and scaled our systems accordingly.

In this chapter we give a description of the methods used to build the initial models. A full phenomenological and morphological description of the models will be given, as well as results, in order to compare them with real-life ellipticals. These results are compared with previous results from other authors in the discussion section. Results concerning the FP will be given in chapter 8.

3 Initial models

We follow closely the Kuijken-Dubinski (Kuijken & Dubinski 1995) algorithm to build our initial models. This algorithm is based on an iterative way of building the initial model. The starting point is an analytic form for the distribution function (DF), written in terms of known integrals of motion. With this we have equilibrium or near equilibrium models. Self-gravitating models will then be constructed through Poisson's equation:

$$\nabla^2\Psi(R,z) = 4\pi G[\rho_{disc}(R,z) + \rho_{bulge}(R) + \rho_{halo}(R,z)]. \tag{6.1}$$

where the densities are obtained by integrating the DF over velocity. The various components are as follows.

Table 6.1— Initial parameters for dbh and dh models.

model	# halo	ψ_o	v_o		
dbh	30000	-4.6	1.42		
dh	30000	-3.0	1.5		
model	#disc	M_d	R_d	R_{outer}	z_d
dbh	12000	0.867	1	5	0.1
dh	15000	1.5	1	5	0.1
model	# bulge	ρ_b	σ_b		
dbh	6000	14.45	0.714		
dh	0	0	0		

Table 6.2— Initial mass ratios and disc central radial velocity dispersion for dbh and dh models.

model	$(M_{lum}/M_{tot})_{Rout}$	$(M_{lum}/M_{tot})_{total}$	$\sigma_{R,0}$
dbh	0.459	0.241	0.410
dh	0.463	0.129	0.320

The bulge is a King (1966) model, where we have to define three parameters: Ψ_c is the cutoff potential of the bulge, ρ_b is the central bulge density and σ_b characterises the velocity dispersion of the bulge.

The halo is an Evans model (Kuijken & Dubinski 1994), where rotation can be included. For this component we have five parameters. These are: the depth of the potential well Ψ_0, a velocity scale σ_0, a density scale ρ_1, the halo core radius R_c and the flattening parameter q.

Finally, for the disk a Shu (1969) model is chosen, generalized to the third dimension by introducing a third integral, E_z (the energy in vertical oscillations). The disk density is nearly exponential with scale length R_d and truncated at radius R_{out}. The vertical dimension follows a $sech^2(z)$ profile, with vertical scale height z_d.

To actually build the initial models one has to choose particle positions and velocities in accordance with the DF's. Normally one chooses $\sigma_b < \sigma_0$ and $\Psi_c - \Psi_0 < 0$ (where Ψ's are negative) to have the bulge more centrally condensed and more radially confined than the halo. Rotation can be included in the halo by chosing an appropriate value for L_z. In the disk the sharpness of the truncation is given by δR_{out}. Parameters for our models are given in table 6.1.

We have chosen disk-bulge-halo (dbh) model A from Kuijken & Dubinski (1995) as initial condition for the dbh systems. This model is heavy-bulge with a disk-to-bulge mass ratio of 2. A dark matter halo is included in order to match the flat part of the circular speed vs. radius diagram. We show this model in figure 6.1. Note that this model does not have a maximum disk, rather the model is heavy-bulge out to $R = 1.5R_d$ and halo-dominated elsewhere. This choice of a bulge dominated system is different from previous work (see Hernquist 1993, Barnes 1998, Naab & Burkert 2001); these authors use a disk-to-bulge ratio of 3.

The algorithm by Kuijken & Dubinski (1995) is used to build the initial models for the dh systems. In their paper Kuijken & Dubinski do not give a model without halo as an example. We attempted several different values for the initial conditions in order to get a stable system. This proved to be a difficult task. A bulgeless disk is quite unstable to bar

formation (Hernquist 1992). To build this bulgeless model a less concentrated halo and more centrally concentrated disk finally provided us with the more stable configuration. In this configuration the disk is almost a maximal disk (slightly sub-maximal) as can be seen from figure 6.1.

Model parameters are given in table 6.1, which list: model name, number of particles in halo, central potential of halo, maximum circular velocity of halo, number of particles in the disk, mass of the disk, scale length of the disk, cut-off radius of the disk, vertical extent of the disk, number of particles of the bulge, central density of the bulge and central velocity dispersion of the bulge. The bulge was chosen not to rotate. With this choice of heavy-bulge and bulge-less systems we are at the extremes of a sequence of bulge-lo-disk ratios resembling the Hubble sequence.

Figure 6.1 gives the initial velocity curves for the two models as well as the Toomre stability parameter, Q, and the surface brightness profiles for the luminous components. The initial velocity curves show the contribution to the total velocity curve (solid line) from the different components. In the dbh model (left panels), the central parts are dominated by the bulge (dot-dashed line). The disk (dashed line) and halo (dotted line) contribute more to the velocity curve from about 1.5 disk scale lengths outwards. The total velocity curve is quite flat between about 1 to 4 disk scale lengths. For dh, disk stability in the absence of a bulge requires a more centrally-concentrated disk. This can easily be seen in the velocity curve where up to 3 disk scale lengths the disk dominates over the halo. For both the dbh and dh models the Toomre stability parameter, Q is flat for a great part of the disk. Both dbh and dh models show similar surface density profiles near the center. These are clearly not exponential. In dbh this is due to the presence of the bulge.

3.1 Units

We use model units so that the constant of gravity is $G = 1$. The total mass of the smallest system is taken to be $M = 1$. The scale length of the smallest disk is $R_d \simeq 0.2$. A set of physical units that match the dbh models to the Milky Way are:

$$[M] = 3.24 \times 10^{11}\ \mathrm{M}_{\odot}, \tag{6.2}$$

$$[L] = 14.0\ \mathrm{kpc}, \tag{6.3}$$

$$[T] = 4.71 \times 10^{7}\ \mathrm{yr}, \tag{6.4}$$

with

$$[v] = 315\ \mathrm{km/s}. \tag{6.5}$$

These units can also be used for dh models.

3.2 Stability of initial models

The stability properties of the dbh and dh models are analyzed by studying the time evolution of key structural properties such as the global mass distribution, the disk thickness and the circular velocity.

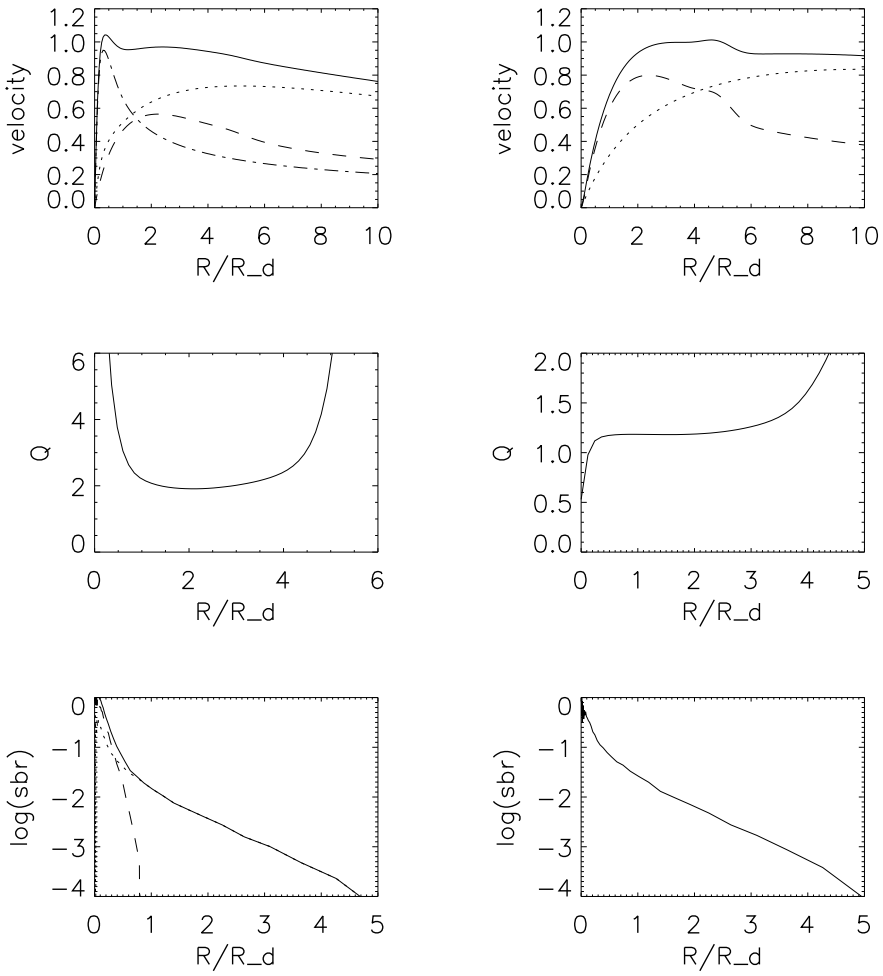

Figure 6.1— Left panels show the velocity curves (top), Toomre parameter, Q, (middle) and the surface brightness profile for the luminous components (bottom) for dbh models. Right three panels show the same quantities for dh models.

Tests with models of galaxies in isolation have been run to test the stability of the initial realizations. These runs last for about 25 half-light crossing times of the disk galaxy. This is less than the duration of the merging models but it is of a comparable scale.

Figure 6.2(a) shows the evolution of the radii enclosing given percentages of the total mass. We see that both at small radii and in the outer parts, the stability is excellent. Figure 6.2(b) gives the final circular velocity curve, i.e. $V_c = \sqrt{GM(r)/r}$,at the end of the run. Figure 6.2(c) gives the evolution of the vertical scale height, which compares well with the results shown by Kuijken & Dubinski (1995) in their figure 7. Test models for dbh systems show that bulge, disk and halo are stable for the duration of the models, disk thickening is quite low as shown in figure 6.2 and the density profile of the bulge is maintained.

Bulgeless models have also been tested for stability. Figure 6.3 shows the same quantities for a test of model dh. Over 35 half-light crossing times the system suffers a mild reorganization of the mass distribution. The disk shows some transient spiral features but is stable against bar formation. Figure 6.3(a) shows the evolution with time of fractional mass radii. Figure 6.3(b) shows the final circular velocity curve, to be compared with the one in figure 6.1. We find that after relaxation the curves have not changed much. Figure 6.3(c) shows that the thickness of the disk is fairly stable.

3.3 Scaling rules

In order to scale models with different masses we derive a scaling law from the Tully-Fisher (TF) relation, and make three additional assumptions on the scaling of masses and typical velocities of the systems. According to the TF relation, the maximum of the velocity curve scales as a certain power of the luminosity of the galaxy:

$$L = AV_{max}^{\alpha}, \tag{6.6}$$

where A is a proportionality constant and α ranges from 2.5 (Ziegler et al. 2002) for the B-band for distant galaxies, to 3.2 for the B band, 3.5 for R and 4 for the I band (Sakai et al. 2000) for nearby galaxies.

Now, if we suppose that these systems are close to virial equilibrium:

$$2E_T = -E_W. \tag{6.7}$$

So:

$$V^2 \propto \frac{GM_{tot}}{R_G}, \tag{6.8}$$

where V^2 is twice the kinetic energy per unit mass of the galaxy and R_G is the gravitational radius that can be derived from the potential energy of the galaxy.

Now we suppose that the luminous mass scales with the luminosity (so we assume $M_{lum}/L = constant$), then:

$$M_{lum} \propto V_{max}^{\alpha} \tag{6.9}$$

With $V \propto V_{max}$ we may eliminate the velocity from these last two equations and find:

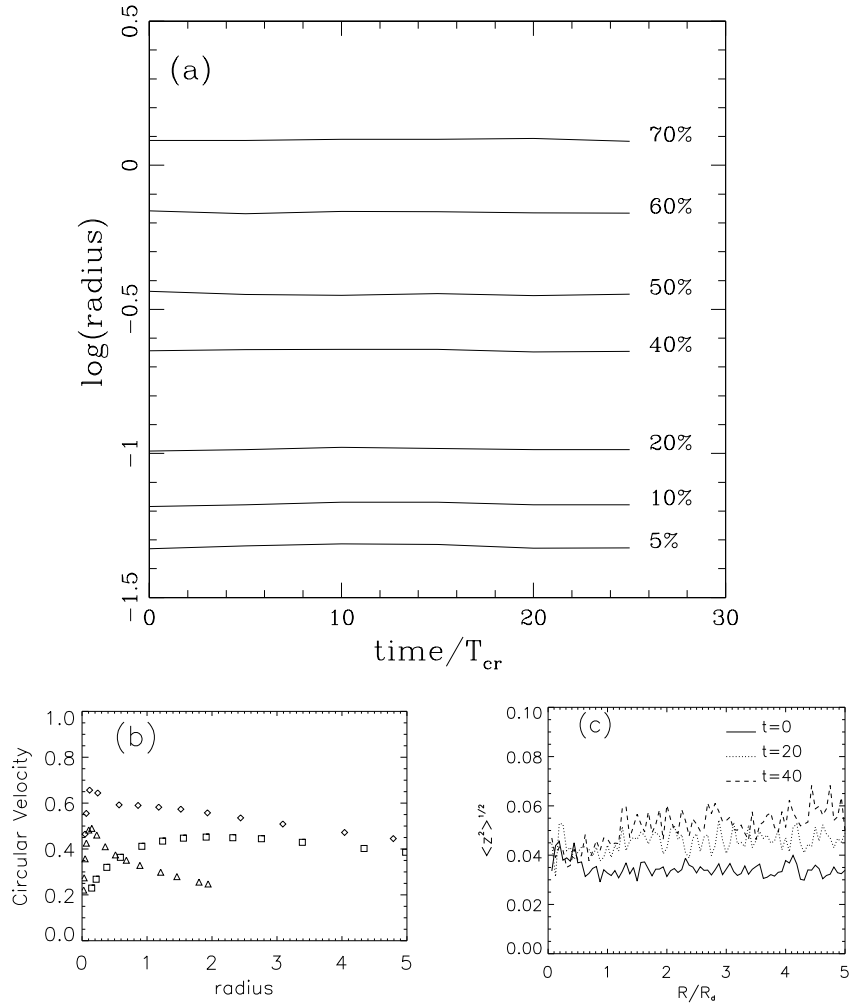

Figure 6.2— (a) Evolution of the radial mass distribution for the initial dbh model, stability is quite good. (b) The final circular velocity for the total mass (diamonds), the bulge (triangles) and for the disk (squares). (c) Evolution of the thickness of the disk during this test.

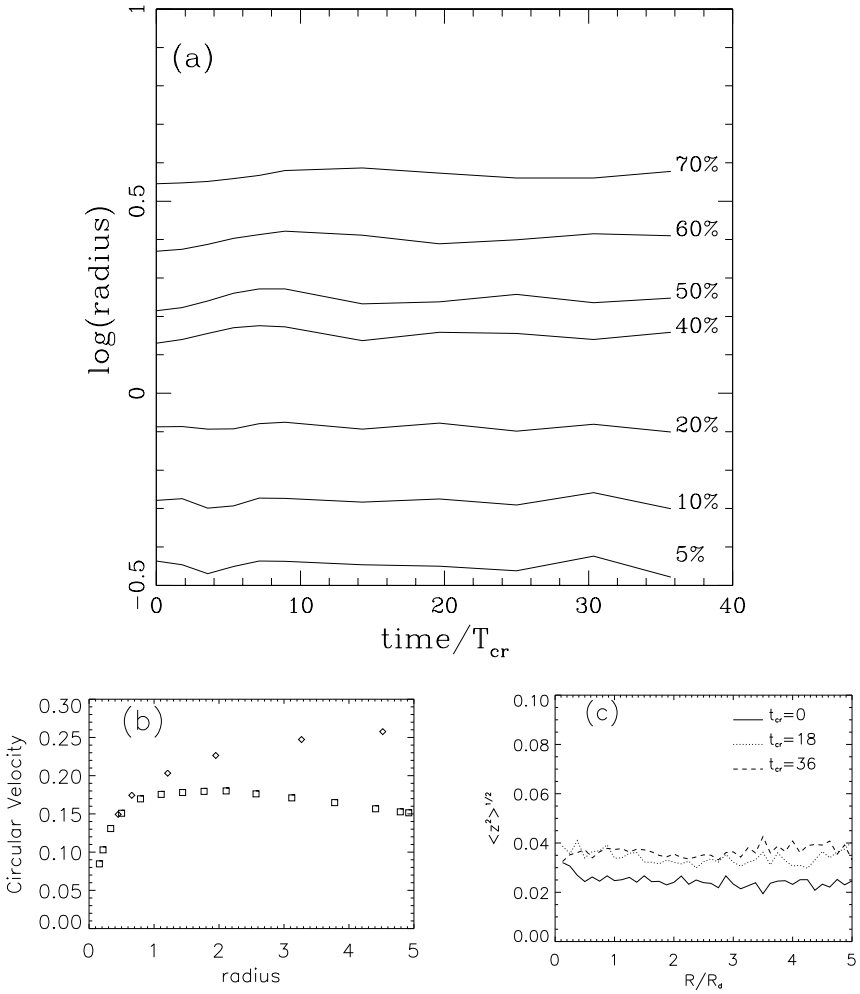

Figure 6.3— (a) Evolution of the radial mass distribution for the initial dh model. The model is fairly stable. (b) The final circular velocity for the total mass (diamonds) and for the disk (squares). (c) Evolution of the thickness of the disk during this test.

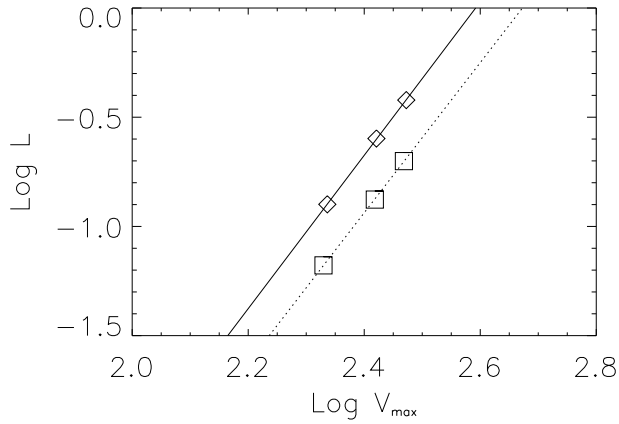

Figure 6.4— Luminosity versus maximum rotation velocity. The luminosity is taken equal to the luminous mass (bulge+disk in dbh models and disk in dh models). Diamonds are dbh models. Solid line is a fit to those points. The slope of this line is 3.51. Squares are dh models and the dotted line is a fit to these points; it has a slope of 3.45.

$$\frac{M_{tot}}{R_G} \propto M_{lum}^{2/\alpha} \tag{6.10}$$

Finally, we assume for our models that $M_{total}/M_{lum} = constant$. Then we obtain our scaling law:

$$\frac{R_1}{R_2} = \left[\frac{M_1}{M_2}\right]^{1-2/\alpha}. \tag{6.11}$$

This scaling depends on the choice of α. Note that for $\alpha = 4$ we obtain Fish's law (Fish 1964). We use collisionless models for our simulations. Extinction is lowest for the far red (R-band). In this band α is close to 3.5-4 (Sakai et al. 2000). The value we have chosen is 3.5.

We have checked whether the models scaled with this procedure actually follow a Tully-Fisher relation. Results are shown in figure 6.4. Initial models do follow a TF like relation. The observed shift between the two relations (i.e. change in the zero-point) is due to the different masses of the luminous parts. Although the total mass in each model is equal to 1, 2 or 3, the different M_{total}/M_{lum} between bulge and bulgeless models gives this shift.

3.4 Merger simulation details

In all simulations two dbh or two dh galaxies are placed on a nearly parabolic, inter-penetrating orbit in the (x, y)-plane. The ellipticity of the orbit is chosen to be $e = 0.7$. Orbital parameters are not changed from one simulation to another since what we want to address is how the change of structure of the initial models affects the final models, not the effect of the orbital parameters. The line connecting the galaxies initially is taken as

the x-axis while the orbital angular momentum defines the z-axis. θ_i and ϕ_i describe the disk spin orientation in spherical coordinates. The relative orientation of the various spin vectors involved can have some effect on the final central velocity dispersion of the merged system. We have done three experiments for each set of mass ratios. In the first set both galaxies rotate with their spin parallel to the orbital angular momentum, but not exactly coupled with it there is a certain angle between them. In the second set, the spin of one of the galaxies is coupled with the orbit while the other is slightly anti-parallel to it. And in the final one both galaxies are placed with their spins anti-parallel to the orbital angular momentum. We will refer to these later as prograde (p), anti-parallel (a) and retrograde (r). For non-equal mass anti-parallel mergers the spin vector of the large system is parallel to the orbit, leaving the smaller one anti-parallel.

Merger simulations are run using Hernquist's version of the TREECODE (Hernquist 1990) on an Ultra Spark Station. Softening is always set to one-fifth of the bulge half-mass radius for the smallest galaxy in each simulation, $\varepsilon = 0.02$ for dbh models, and to one-fifth of the disk half-mass radius for dh models, $\varepsilon = 0.09$. The tolerance parameter is set to 0.8, and quadrupole terms are included in force calculation. Individual time step calculation is included.

We have modeled the bulge with 6000 particles, the disk with 12000, and the halo with 30000 particles for dbh models. For dh models the disk has 15000 particles and the halo has 30000 particles. These particle numbers are rather low but they are comparable to Barnes (1992) and Hernquist (1992, 1993) and not so different from later work by these authors and others (Hernquist et al. 1996, Naab et 1999). In his article Barnes uses from 32768 up to 65536 particles. Our models include 48000 and 45000 particles in each galaxy, this means 96000 and 90000 particles in the whole system. In the choice of particle numbers we took into account that the particle masses for the various components were as similar as possible to avoid for particle-particle heating. The maximum ratio of particle masses is 7.5 for dbh models and 11.6 for dh models.

Systems are let to relax after merger for at least 40 half-light radius crossing times. Energy conservation errors are kept below 1%.

Table 6.3 gives the initial parameters for our runs. The first column provides the model name. The first nine rows give dbh models, while models with an asterisk symbol are dh models. The number indicates the mass ratio of the initial systems and the final letter the relative orientation of the spins with respect to the orbital angular momentum: p means prograde, a means anti-parallel and r means retrograde. The second column gives the masses of the initial systems. M_2 denotes the largest system, the smallest system has mass 1 in all cases. The third column gives spin orientation relative to a system of axes where the orbital angular momentum is parallel to the z-axis while the systems are initially placed along the x-axis. The next columns give the initial separation, orbital ellipticity, pericenter distance and pericenter time for the Keplerian orbit with the same initial parameters.

4 Results

We have run 18 simulations all ending in a merger. They display a wide variety of morphological, kinematic and 'photometric' characteristics that will be described in this section.

Table 6.3— Input configurations for disc-bulge-halo models (first 9 entries) and for disc-halo models (maked with *).

Model	M_2/M_1	(θ_1,ϕ_1),(θ_2,ϕ_2)	$R_i = a$	e	R_{peri}	T_{peri}
$1p$	1:1	(10,-10);(70,30)	11.25	0.7	3.38	23.23
$1a$	1:1	(130,60);(70,30)	11.25	0.7	3.38	23.23
$1r$	1:1	(170,-10);(110,30)	11.25	0.7	3.38	23.23
$2p$	2:1	(10,-10);(70,30)	24.76	0.7	7.43	61.94
$2a$	2:1	(130,60);(70,30)	24.76	0.7	7.43	61.94
$2r$	2:1	(170,-10);(110,30)	24.76	0.7	7.43	61.94
$3p$	3:1	(10,-10);(70,30)	26.98	0.7	8.07	60.99
$3a$	3:1	(130,60);(70,30)	26.98	0.7	8.07	60.99
$3r$	3:1	(170,-10);(110,30)	26.98	0.7	8.07	60.99
Model	M_2/M_1	(θ_1,ϕ_1),(θ_2,ϕ_2)	$R_i = a$	e	r_{peri}	T_{peri}
$1p*$	1:1	(10,-10);(70,30)	12	0.7	3.60	25.60
$1a*$	1:1	(130,60);(70,30)	12	0.7	3.60	25.60
$1r*$	1:1	(170,-10);(110,30)	12	0.7	3.60	25.60
$2p*$	2:1	(10,-10);(70,30)	20	0.7	6.00	44.97
$2a*$	2:1	(130,60);(70,30)	20	0.7	6.00	44.97
$2r*$	2:1	(170,-10);(110,30)	20	0.7	6.00	44.97
$3p*$	3:1	(10,-10);(70,30)	22	0.7	6.60	44.93
$3a*$	3:1	(130,60);(70,30)	22	0.7	6.60	44.93
$3r*$	3 :1	(170,-10);(110,30)	22	0.7	6.60	44.93

4.1 Phenomenology and morphology of the final systems

The morphological features of the final systems depend on the orientation parameters , on the initial mass ratio of the merging galaxies and on the presence or absence of a bulge component. We describe here the main features and their dependence on these parameters.

Figure 6.5 shows the time evolution of the luminous matter in model $1p$. The point of view is parallel to the orbital angular momentum vector. The systems come to the first pass through the pericenter around $t = 20$ after that they separate developing tidal tails and a bridge of particles. Apocentre is reached around $t = 40$ and the systems merge around $t = 60$. At time $t = 80$ the simulation was stopped.

Figure 6.6 shows the time evolution of the luminous matter in the bulgeless model $1p*$. The systems come to the first pass through the pericenter around $t = 25$ after which they separate developing tidal tails. When we compare this evolution with the bulge dominated system $1p$ (see figure 6.5) we find that the tails are not so prominent and that the central parts of the bulgeless systems appear to develop a bar, which was also noticed by Hernquist (1992). At the last frame shown the systems are not fully merged yet, so they were let to evolve further. At time $t = 200$ the simulation was stopped.

Figure 6.7 shows the final state of model $1a$ in different frames. The first one shows this system with an aperture of 20 scale lengths. Inside this radius up to 98% of the total luminous mass is included. The next two frames are close-ups with an aperture of 5 lengths; this includes up to 70% of the total mass. One frame shows a top view (parallel to the orbital angular momentum) and the other a view from the y-axis (perpendicular to both the orbital angular momentum and the line connecting the initial systems). The half-mass radius of the merger remnant is $R_{1/2} = 0.52$.

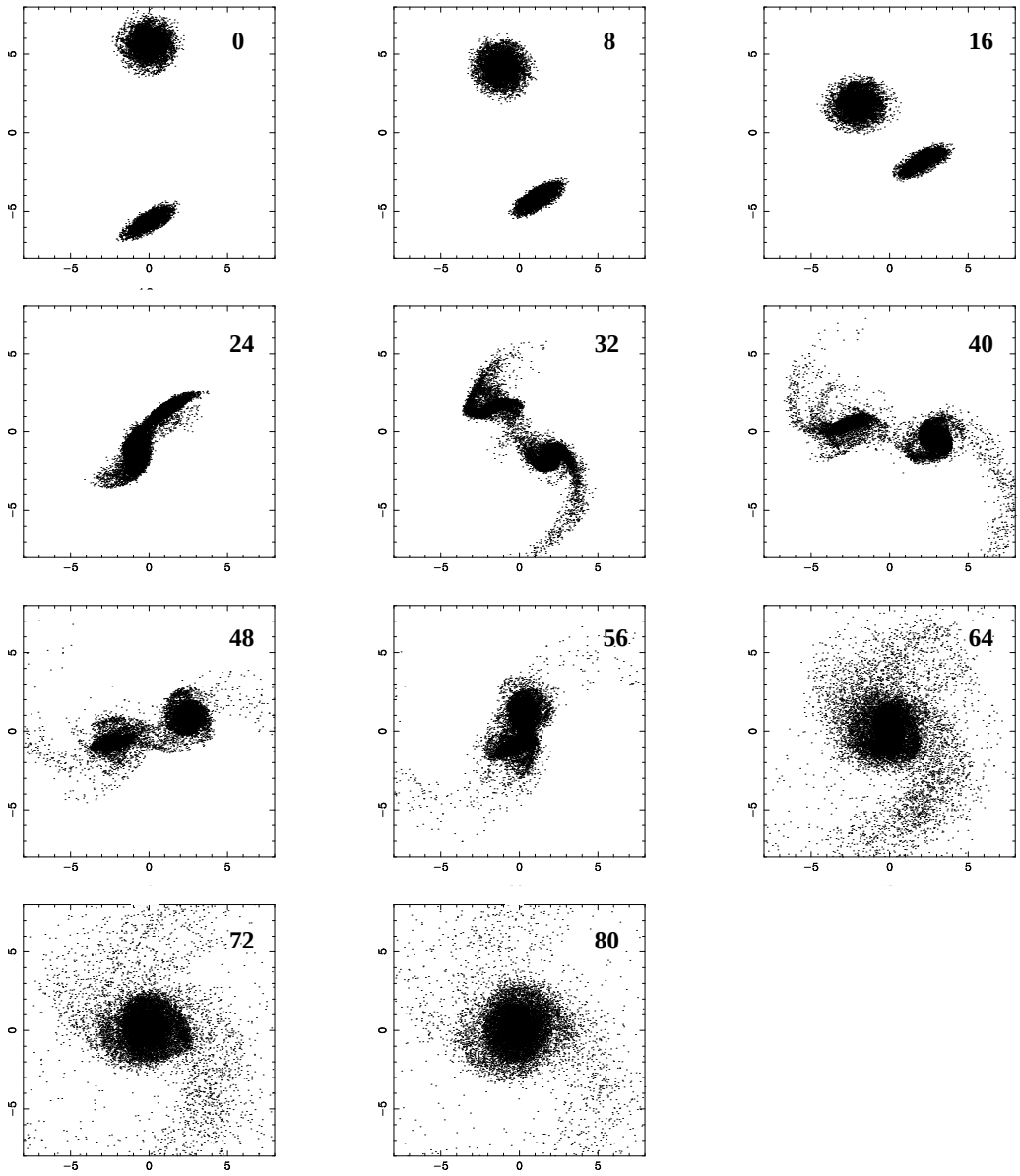

Figure 6.5— Time evolution of the luminous matter in run $1p$ of the disk-bulge-halo series. Time is indicated in the upper right corner. The half mass radius of the final merged system is 0.52.

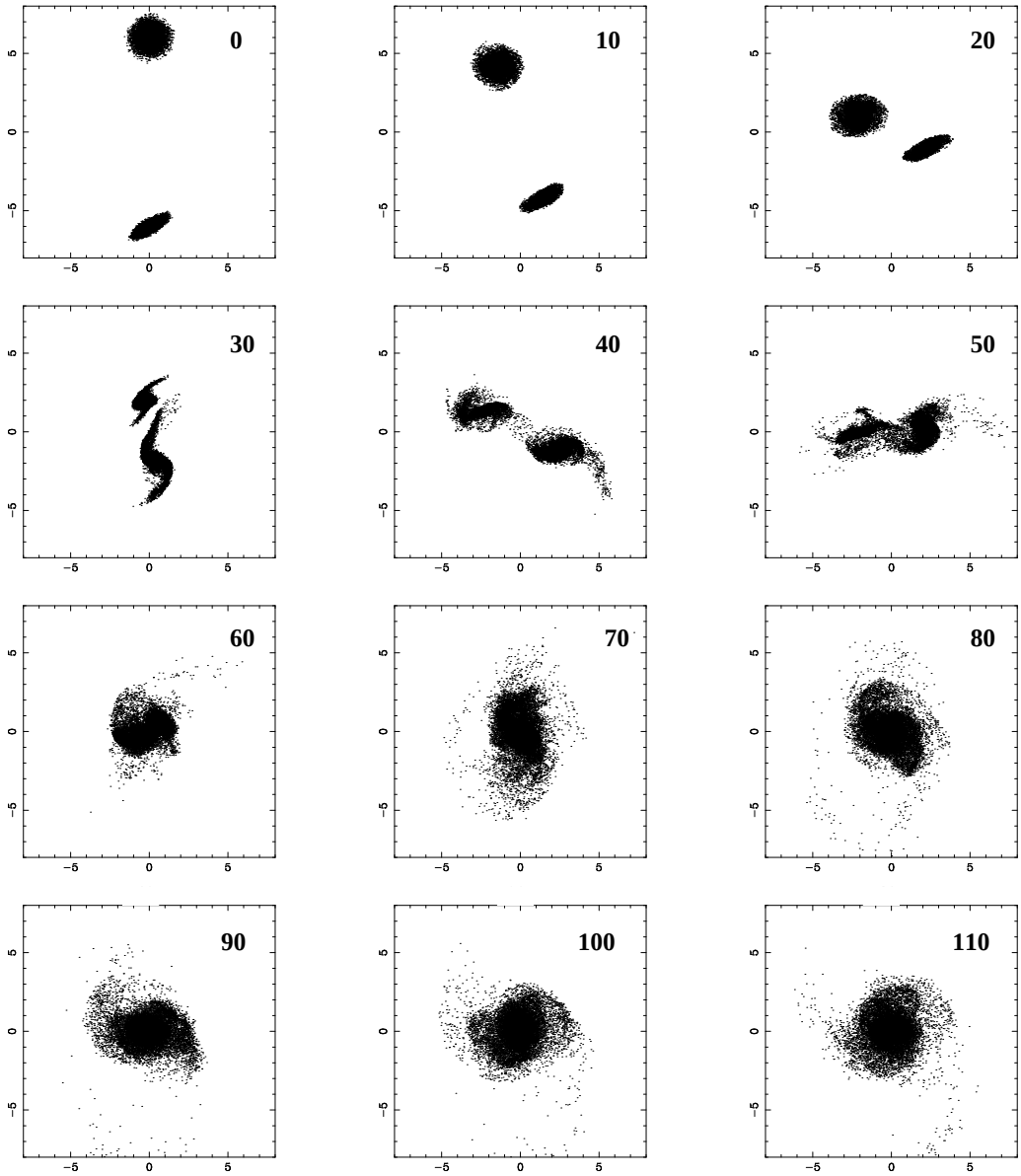

Figure 6.6— Time evolution of the luminous matter in the bulgeless simulation $1p*$, (compare with figure 6.5). Time is indicated in the upper right corner. The half mass radius of the final merged system is 0.57.

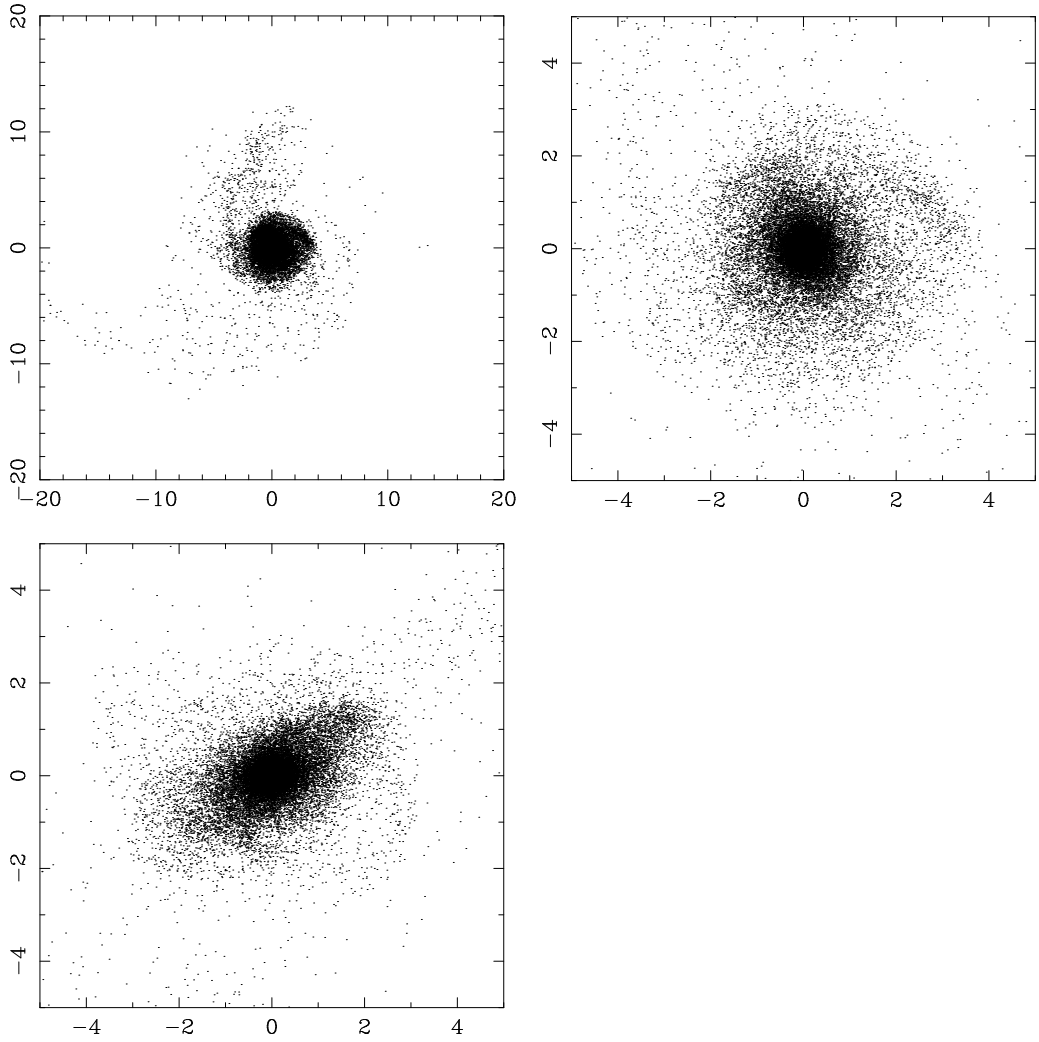

Figure 6.7— Final state of model $1a$ of the dbh series. Top-left panel shows the system up to 20 scale units. This includes about 98% of the luminous mass. The other two frames give two perpendicular views of the same system inside radius 5 (including 70% in luminous mass). Top-right frame is the same point of view as top-left. Bottom panel is a point of view perpendicular to this one.

Tails

Figure 6.8 shows the distribution of the luminous matter at the final time for each of our dbh models. All systems, both prograde and retrograde mergers, show the presence of tails. The longest tails are formed during the first pass through pericenter, as noted by Toomre & Toomre (1972), and Barnes (1992). Prograde (p) systems show more prominent tails than anti-parallel (a) or retrograde (r) in agreement with Barnes (1992) and Hernquist (1993). In the retrograde simulations the tails, although present, are more diffuse.

Prograde simulations show the longest tails for models with similar galaxy masses. The tail appears more sharply defined the greater the mass difference between the initial disks. In parallel simulations with non-equal masses we find a non-symmetrical tail. This tail consist of material from the less massive disk.

In most of the simulations the material in the tails is bound, except in model $1r$ where some of the particles in the more extended tail have a positive binding energy and therefore will escape from the system. Also in that simulation most of the particles eventually return to the main body.

Rather different results hold for bulgeless (dh) systems. Figure 6.9 shows snapshots of the luminous matter distribution at the end of the nine dh simulations, as viewed from the z-axis. Tails in the dh mergers are much less prominent than in the dbh mergers (compare figures 6.8 and 6.9). The merger remnants do not show clear tails at the last computed frame. The only exceptions are prograde, unequal mass mergers (models $2p*$ and $3p*$). These tails extend out to 50 units and the material in them consists of stars from the less massive system. All the material in the tails formed during the merger stages in other configurations has already fallen back to the inner parts while in the prograde and non-equal mass merger this is still to happen.

Shells

Remnants of the dbh systems do not show clear shells. The models in figure 6.8 do not show shells even when plotted at a scale that shows the details of the main body. This may in part be due to the low number of particles. These systems might develop shells later when some of the material that is now forming the tails falls back into the main body.

Remnants of the dh systems, on the other hand, do show shells at the end of the integration for some of the merger configurations. Shells are clearly visible in figure 6.9 for non-equal mass mergers placed in non-parallel orbits. The lack in particle resolution is an obstacle to say something more precise, such as the number of shells and whether they are interleaved in radius. The shells seen in figure 6.9 are of type II (all-round) or type III (irregular) according to the definitions by Prieur (1990). Here we find as well that the geometry of the orbit influences the final configuration of the shells.

These shells can be futher studied in the radial velocity versus spherical radius (V_r vs. R) diagram (see Hernquist & Quinn 1988 and Merrifield & Kuijken 1998, figure 6.10). In this diagram the material that is forming the shell can be seen on sharp V-shaped edges for model $2a*$. We find (see figure 6.11) that similar sharp features can be observed in the two diagrams of V_r vs. E and V_t vs. E. These features do not appear in plots for the dbh models.

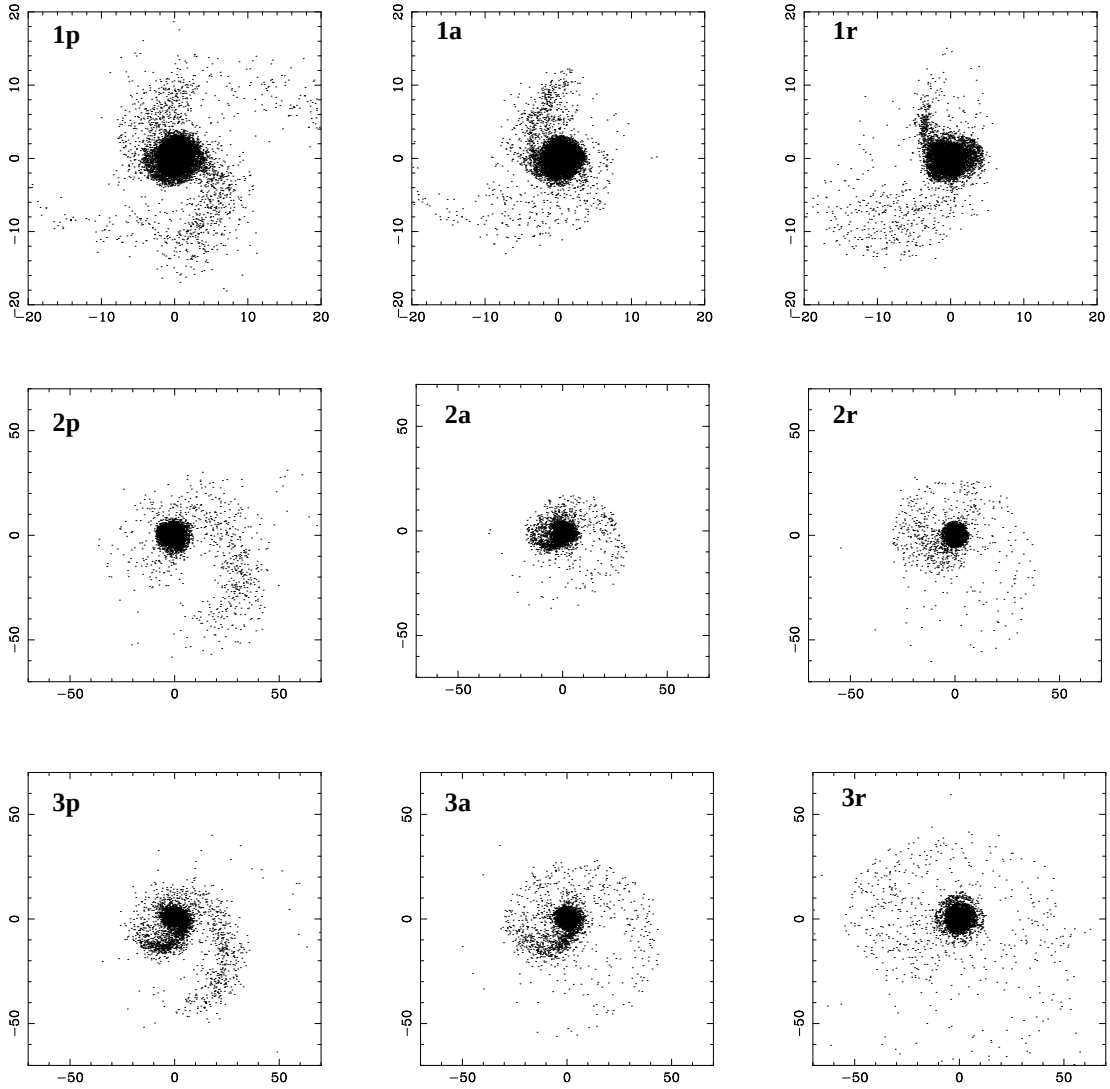

Figure 6.8— Final state of the luminous matter in each of the dbh simulations. Note the difference in extent of the tidal tails.

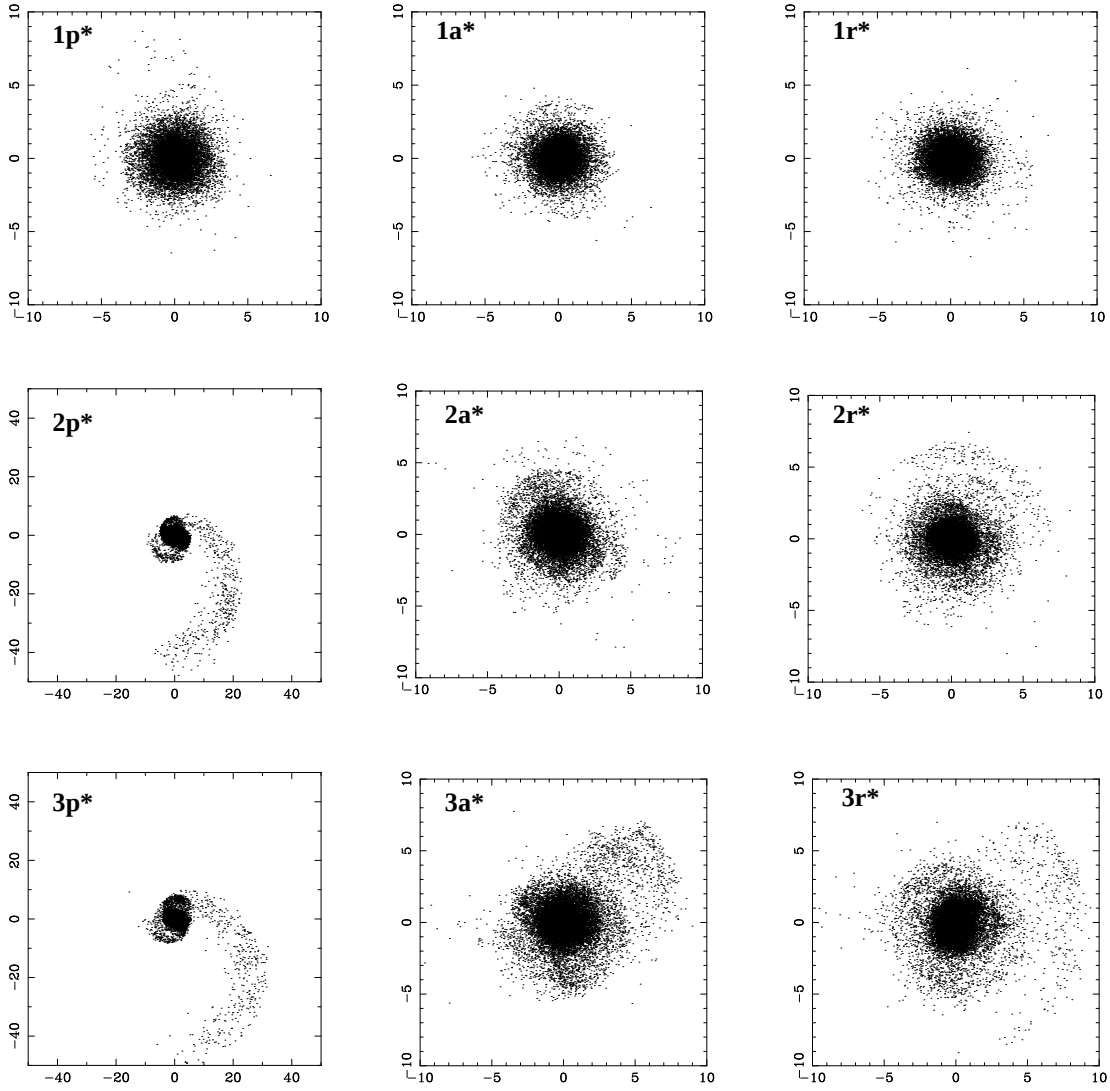

Figure 6.9— Final state of the luminous matter in each of the bulgeless simulations. Note the different linear scales for some models. For details see text.

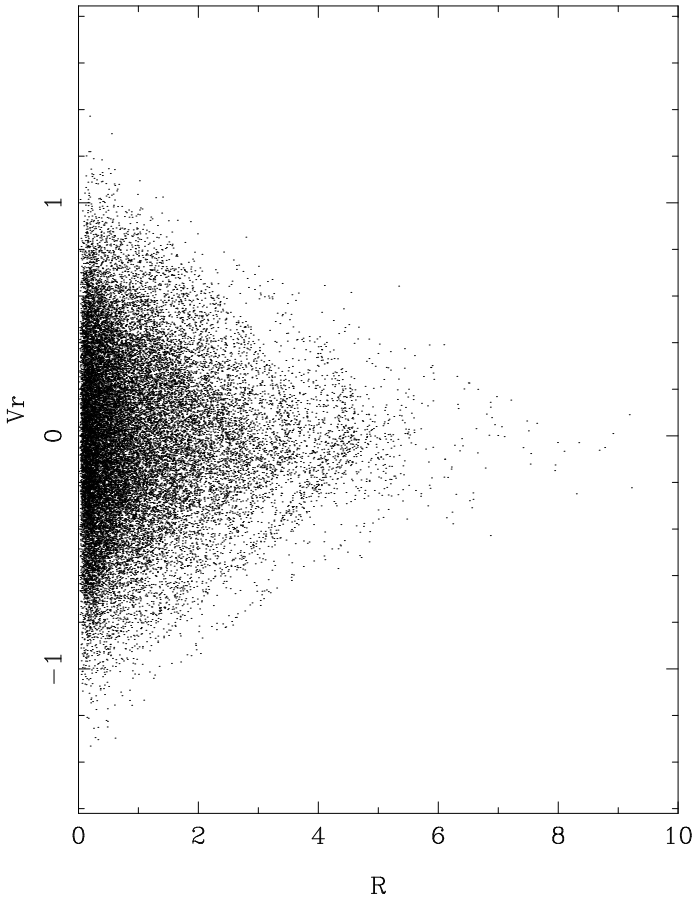

Figure 6.10— V_r vs. R diagram for simulation $2a*$. We find the sharp V-shaped features characteristic of shells formed by phase-wrapping.

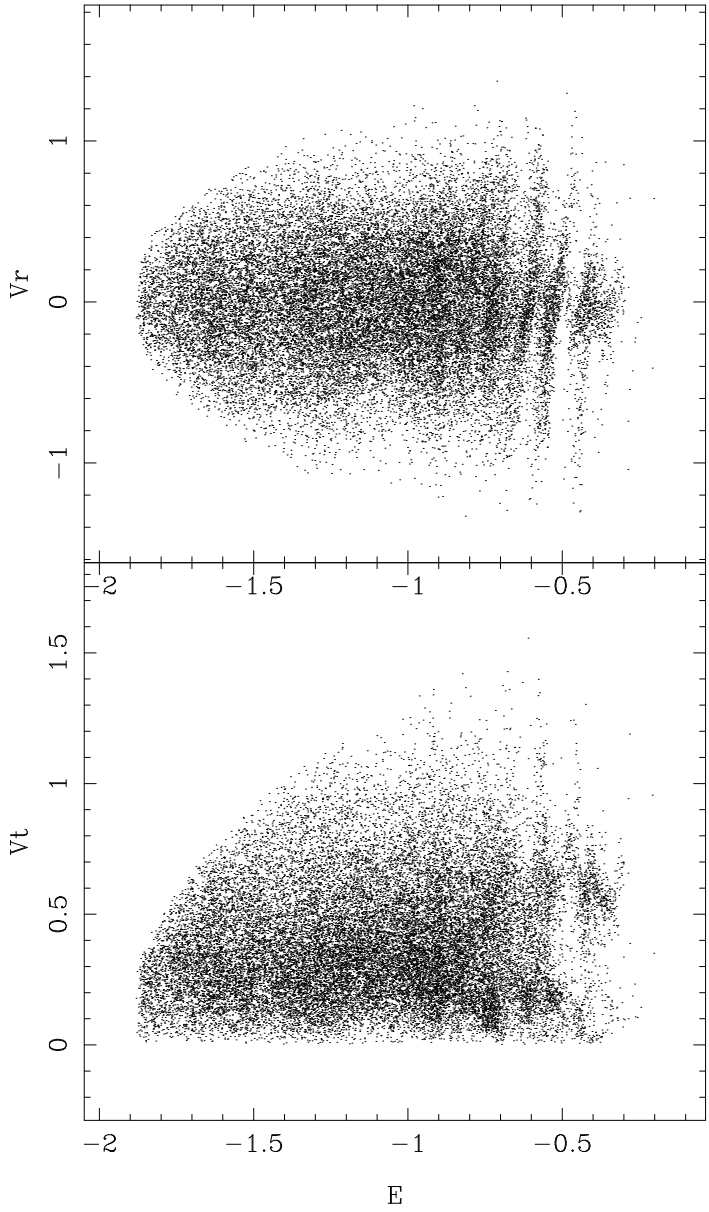

Figure 6.11— Top panel shows the radial velocity of the particles versus their energy for simulation $2a*$. Bottom panel shows the tangential velocity versus the energy of the particles. Note the sharp features in both diagrams.

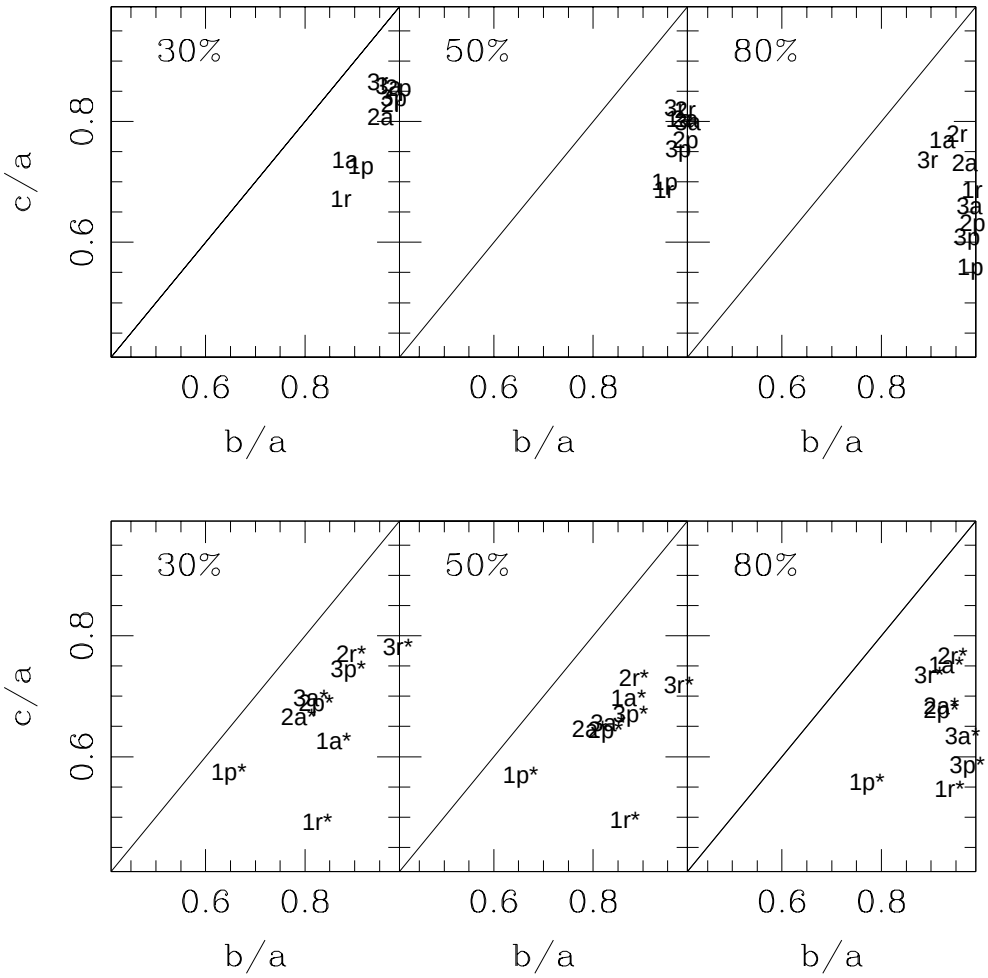

Figure 6.12— Axis ratios of the final models, for three different radii. Top are dbh models, bottom are dh models. Left panels gives axis ratios for a radius including 30% of the luminous mass, the center ones for 50% and the right for 80%.

4.2 Axis ratios

Following the algorithm described in Chapter 2 we have calculated the axis ratios for the final models from the inertia ellipsoid for the luminous matter. We do this for three different radii. These radii include 30%, 50% and 80% of the luminous mass.

The axis ratios for dbh and dh models are plotted in figure 6.12, top and bottom, respectively. The diagrams, used by de Zeeuw & Franx (1991) to study the intrinsic shapes of elliptical galaxies, show b/a vs. c/a (assuming $a > b > c$). In such diagrams, spherical objects ($a = b = c$) lie at the upper right corner, oblate objects lie on the $b/a = 1$ line, and prolate objects lie on the diagonal ($b/a = c/a$).

Models with bulge end up nearly oblate while bulge-less models end up triaxial. Figure 6.12 shows a strong dichotomy of shapes between dbh and dh models. Mergers of dbh galaxies lie very close to the oblate line at all radii (except for a mild triaxiality at small radii for 1:1 mergers), while dh models show strong triaxiality inside the 50% mass radius. All models are oblate at radii including 80% of the luminous mass. In general, we therefore find a trend towards the model becoming more oblate with increasing radius, as previously noted by Gerhard (1983), Barnes (1992) and Hernquist (1992, 1993).

In general we find equal mass mergers to produce the smaller c/a and b/a. Remnants of equal-mass systems are more triaxial than those with mass ratios of 2:1 or 3:1, which lie closer to the oblate systems. This trend is stronger for bulge-less models than for models with bulges.

The type of orbit also affects the final axis ratios. The inner parts of systems coming from parallel configurations look more prolate than other configurations which are closer to triaxial.

A surprising result is the fact that 2:1 and 3:1 merger remnants are closer to the location of spherical systems in figure 6.12 than equal mass merger remnants, for both heavy-bulge and bulge-less systems, contrary to what Barnes (1998) finds.

For bulgeless systems bar formation is more efficient for 1:1 mass ratios and so they end up with more prolate and more flattened shapes. For non-equal mass ratios the interaction with the smaller galaxy heats up the disk leaving an oblate remnant.

4.3 Surface density profiles

We derive surface density profiles from ellipse fits to the isodensity contours of the merger remnants, as viewed from a point of view parallel to the initial orbital angular momentum. Surface density profiles for the nine dbh models are shown in figure 6.13, and for the nine dh models in figure 6.14.

These profiles are fitted using a least-square method to a de Vaucoleurs (1958) profile:

$$I = I_e \exp\{-7.61[(R/R_e)^{1/4} - 1]\}, \tag{6.12}$$

and also to a Sersic (1968) profile:

$$I = I_e \exp\{(-1.9992n + 0.3271)[(R/R_e)^{1/n} - 1]\}. \tag{6.13}$$

In order to avoid softening effects at small radii, we have only fitted points outside $2 \times \varepsilon$, (with $\varepsilon = 0.02$ for dbh models and 0.09 for dh models). Fits exted out to $R = 5$. Best fit

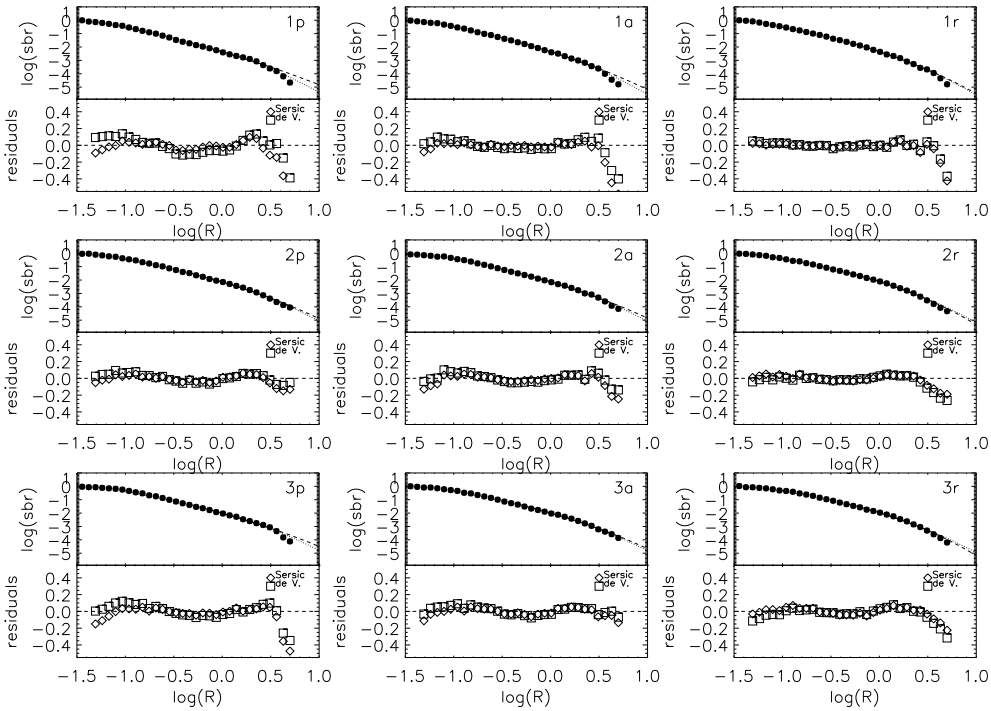

Figure 6.13— Surface density profiles for the nine dbh models. For each plot, the top panel shows the surface density profile as dots. Two fits are done, one with a Sersic profile and a second one with a de Vaucouleurs law. The bottom panel shows the residuals of these two fits to the data. Squares are the residuals from the de Vaucouleurs law, diamonds residuals from the Sersic law.

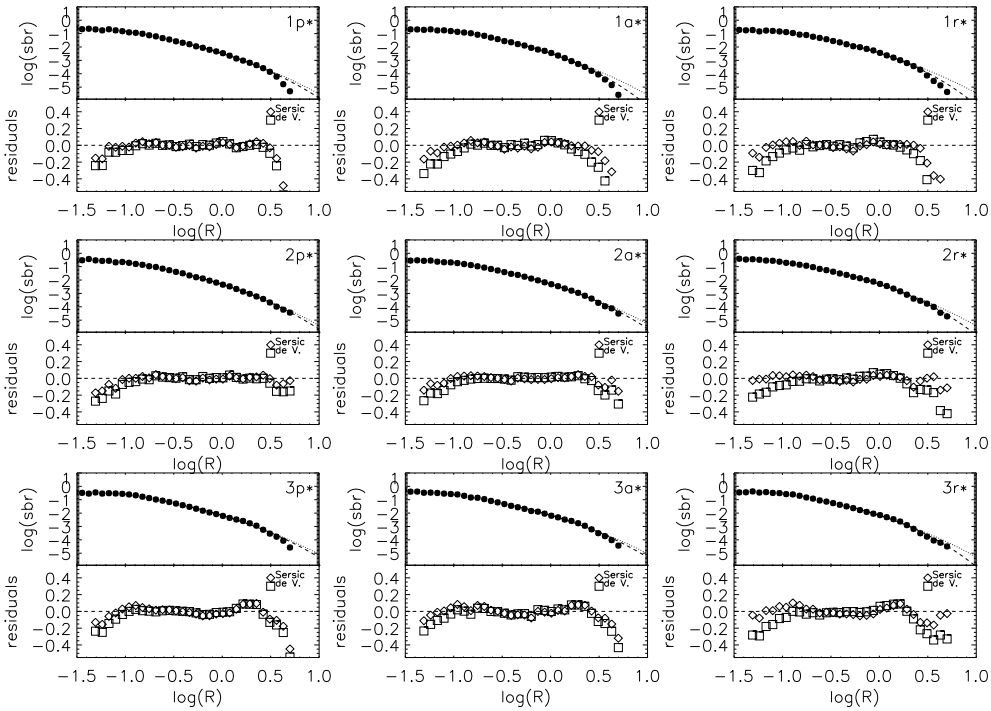

Figure 6.14— Surface density profiles for the nine dh models. For each plot, the top panel shows the surface density profile as dots. Two fits are done, one with a Sersic profile and a second one with a de Vaucouleurs law. The bottom pannel shows the residuals of these two fits to the data. Squares are the residuals from the de Vaucouleurs law, diamonds residuals from the Sersic law.

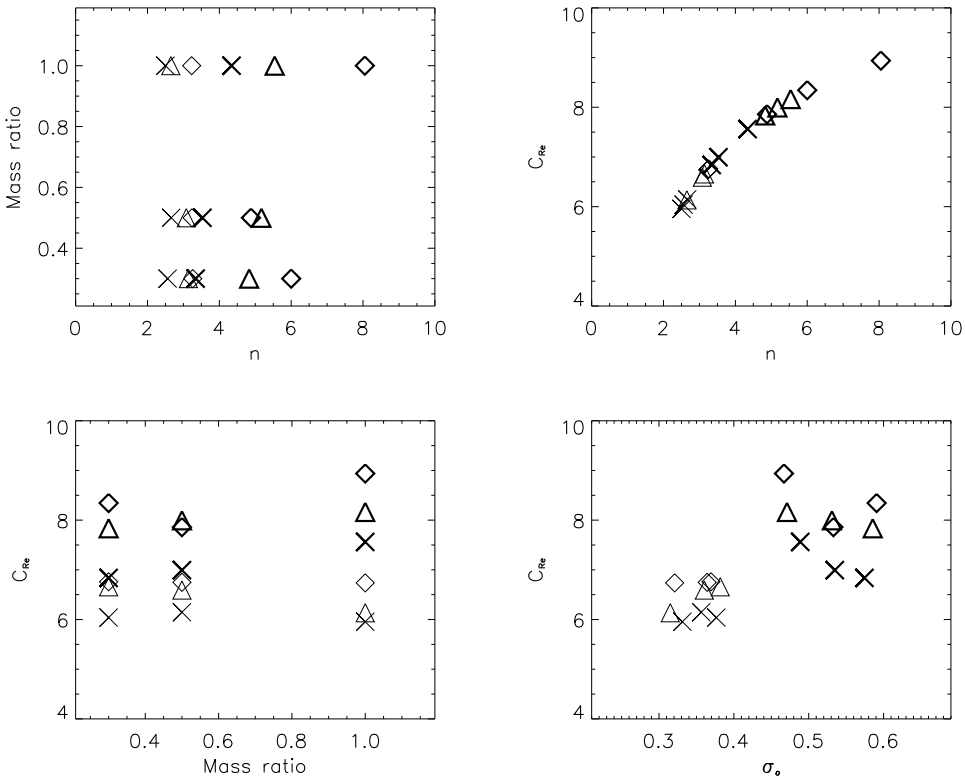

Figure 6.15— Observed properties of the merger remnants, identified as in table 6.3. Top left: mass ratio versus index n of Sersic profile fit. Top right: Trujillo et al (2001) concentration parameter C_{Re} versus n. Bottom left: C_{Re} versus mass ratio. Bottom right: C_{Re} vesus central velocity dispersion. The two sets are shown by the different thickness of the symbols, the thickest are dbh models. Diamonds are 'p' models, triangles are 'a' models and crosses are 'r' models.

parameters for Sersic and de Vaucouleurs fits are given in table 6.4. In figures 6.13 and 6.14 the bottom panel for each of the plots gives the residuals for both fits.

In general our surface density profiles are well approximated by a de Vaucouleur's profile. This is especially true for the inner regions. A slightly better fit can be achieved with the Sersic profile. Looking at the results of this fit we find that models with bulge give results with exponents closer to 4 than for the fits for the bulgeless remnants. Merger remnants originating from bulgeless systems give exponents between $n = 2.4$ and $n = 3.2$, while dbh systems yield $n = 3.3$ and $n = 6$. The lower Sersic indices of the dh models are probably a result of the lower central densities of the initial models.

The orbital configuration also affects the final profile. In general prograde and antiparallel configurations give a higher value for n than orbits where both spins are opposite to the orbital angular momentum. This is true for both dbh and dh models. The mass ratio does not have a significant effect on n.

Table 6.4— Best-fit parameters for Sersic and de Vaucouleurs fits to the surface density profiles. For each model, the first line gives the best-fit parameters for a Sersic profile, and the second line the parameters for a de Vaucouleurs fit ($n = 4$).

Model	$\log(I_e)$	R_e	n	**Model**	$\log(I_e)$	R_e	n
$1p$	-1.779	0.519	8.05	$1p*$	-1.937	0.545	3.23
	-1.700	0.505	4.00		-1.953	0.549	4.00
$1a$	-1.538	0.407	5.54	$1a*$	-1.802	0.491	2.65
	-1.538	0.423	4.00		-1.851	0.494	4.00
$1r$	-1.492	0.398	4.34	$1r*$	1.892	0.552	2.50
	-1.497	0.404	4.00		-1.969	0.574	4.00
$2p$	-1.691	0.601	4.88	$2p*$	-1.748	0.533	3.24
	-1.674	0.602	4.00		-1.738	0.519	4.00
$2a$	-1.666	0.584	5.17	$2a*$	-1.826	0.593	3.08
	-1.649	0.585	4.00		-1.838	0.586	4.00
$2r$	-1.526	0.525	3.53	$2r*$	-1.691	0.520	2.66
	-1.538	0.523	4.00		-1.682	0.496	4.00
$3p$	-1.769	0.758	6.00	$3p*$	-1.802	0.654	3.26
	-1.709	0.724	4.00		-1.802	0.646	4.00
$3a$	-1.682	0.698	4.83	$3a*$	-1.838	0.689	3.14
	-1.666	0.697	4.00		-1.851	0.686	4.00
$3r$	-1.481	0.583	3.34	$3r*$	-1.604	0.545	2.56
	-1.487	0.574	4.00		-1.563	0.498	4.00

In figure 6.15 we have plotted several observables. We include here the concentration index, C_{R_e}, defined in Trujillo et al. (2001) as the ratio between the light within $0.3R_e$ to the light within R_e, where R_e is the effective radius derived from the Sersic's fit. C_{R_e} is a monotonic function of n (see figure 6.15, top-right panel). The concentration index C_{R_e} is distinctly higher for dbh models than for dh models. Clearly, the presence of the bulge in the progenitors leads to a higher central concentration in the light distribution of the remnants, indicating that the concentration of the remnant is a tracer of the concentration of the precursors. Higher central concentrations are associated to higher central velocity dispersions (figure 6.15, bottom-right panel), as found for real ellipticals by Graham et al. (2001).

For all the systems, the profiles deviate from both the de Vaucouleur and the Sersic laws at the outermost radii.

4.4 Boxiness-diskiness

As considered before in Chapters 2 and 4 we calculate the boxiness-diskiness of the isophotal profiles of our merger remnants. We do this by calculating the deviation $\delta(\phi)$ from pure ellipses:

$$\delta(\phi) = \delta + \sum a_n cos(n\phi) + \sum b_n sin(n\phi), \tag{6.14}$$

where ϕ is the azimuthal angle sweeping around the ellipse, $\delta(\phi)$ is the residual intensity along the best-fitting ellipse, δ is the mean residual intensity and $n = 1, 2, ...$ For well behaved isophotes, δ, a_1, a_2, a_3 and the b_n should be small. The deviations were measured as

residuals of the intensity along the ellipse. Isophotes are called disky when a_4 is positive, and boxy when a_4 is negative (see Binney & Merrifield 1998).

In figure 6.16 we show how the a_4 parameter varies with projected radius for several models. We have calculated this quantity from a point of view parallel to the intermediate axis of the inertia ellipsoid, measured at the half-light radius for each model. In order to improve the signal-to-noise ratio an average over 60 snapshots was taken. In general deviations are quite small.

The left row in figure 6.16 gives dbh models, while the right one gives dh models. For dbh models we observe different behaviour depending on the initial mass ratio. In general, from this point of view, equal mass mergers appear boxy, while when the mass ratio is increased the final system appears more disky. This is in agreement with Naab et al. (1999).

For dh models the inner parts (up to $2R_e$) are in all cases boxy while the outer parts show disky deviations.

We have studied the variation of the a_4 parameter from one hundred random points of view. Boxiness-diskiness has been claimed to be point of view dependent (Fasano 1991, Stiavelli et al. 1991, Ryden 1992, Governato et al. 1993, Heyl et al. 1994, this thesis chapter 2). We have done these measurements for model $3r$ for radii out to $3R_e$. Inside this radius the remnant is fully virialized and is not showing clear features such as tails and plumes, that may contaminate the isophotal profiles. Profiles are expected to vary only slightly as a result of late in-falling of merger debris.

In figure 6.17 a histogram of a_4 for model $3r$ is given. The a_4 values given here are mean values of the diskiness-boxiness inside $1.5R_e$ and $3R_e$ for one hundred points of view. To improve the signal-to-noise ratio an average over 60 snapshots was taken.

Both figures 6.16 and 6.17 show that the a_4 values are comparable to those observed in real galaxies. Figure 6.17 shows that depending on the point of view a system can be seen as either boxy or disky. Increasing the aperture, in the case presented in figure 6.17, does have an effect on how the system would be classified.

4.5 Kinematics

Rotation curves

We will examine at the rotation curve as seen from the y-axis. This is the axis perpendicular to the orbital angular momentum and the line connecting the two initial systems. From this point of view we take a logarithmic grid and bin the particles within it. This provides a pixelized image and with it we have calculated the isophotes, fitting an ellipse to them. Then, we determine the major and minor axes. We measure the rotation curves along the major as well as the minor axis. The slit, which passes through the center of the galaxy has a total lenght of 2 and a width of 0.3. With this choice, we map the rotation curves out to a radius enclosing 70% of the projected mass. Comparison with the values of the effective radius in table 6.4, shows that this choice takes the rotation curves at least to $2R_e$. Major- and minor-axis rotation curves are shown in figure 6.18 for all models. Figure 6.19 shows the maximum of each rotation curve V_{max} vs. the progenitor mass ratio.

Figure 6.18 clearly shows that all merger remnants show rotation about the major axis. The amplitude of the rotation curve depends on the mass ratio of the initial systems. This is seen in figure 6.19. However for a given mass ratio the different orbital configurations also affect the amplitude of the rotation curve. Retrograde models, both with and without

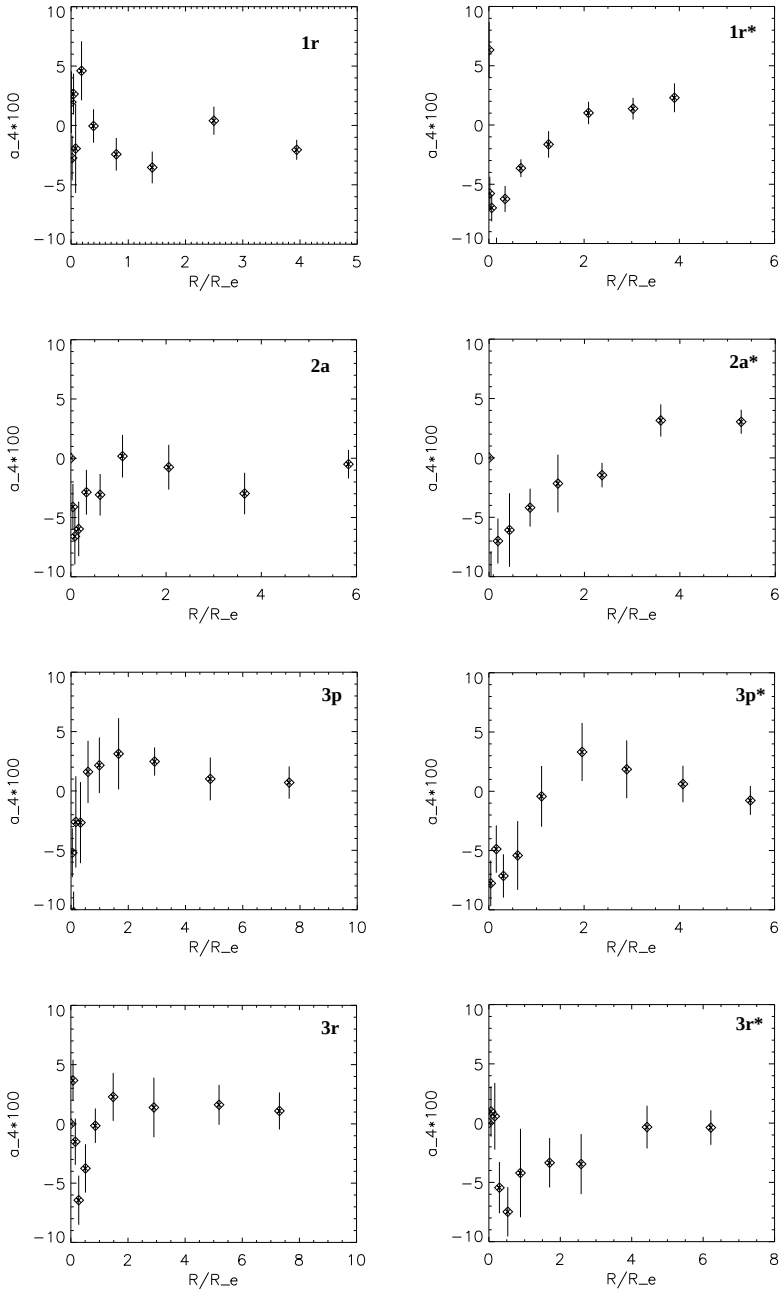

Figure 6.16— Boxiness-diskiness, as measured by $100a_4$, vs. R/R_e for several models. The point of view is parallel to the intermediate axis at the half-light radius of the remnant. Models names are given.

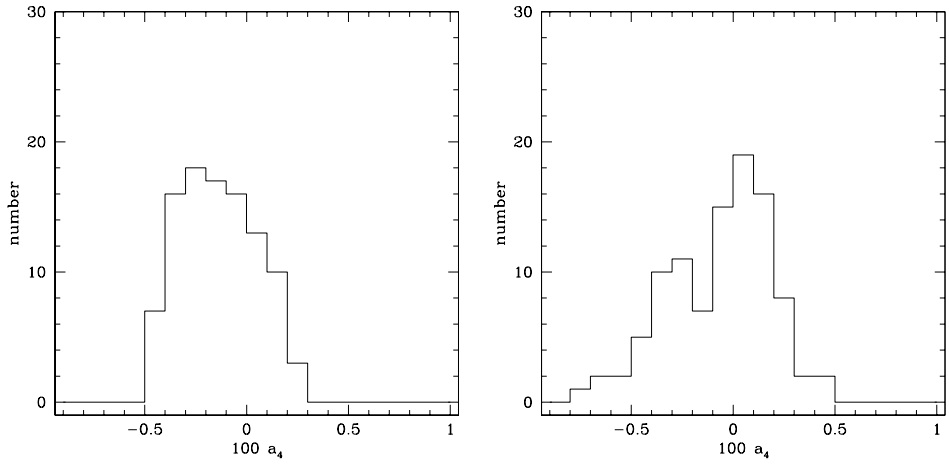

Figure 6.17— Histograms of boxiness distribution for model $3r$. We have calculated the mean a_4 parameter inside $1.5R_e$ (left) and $3R_e$ (right) of this model as measured from one hundred points of view (randomly chosen) for 60 snapshots .

bulge, show counter-rotation for the outer parts -not shown in figure 6.18- as noted before by Balcells & González (1998). Figure 6.18 shows the effect of having a bulge or not: systems resulting from bulgeless progenitors appear to have less rotation in general than those resulting from progenitors with bulge, also seen in figure 6.19.

A particular model seems to be 3r*, shown in the right most panel in the second row. This model shows a profile with little rotation and a mild counter-rotation in the inner parts. This model has a retrograde orbit and therefore has an initial configuration similar to those of Balcells & González (1998).

On the other hand, neither bulge nor bulgeless systems appear to have significant rotation about the minor axis. However, for some configurations, mergers of heavy-bulge systems yield a small minor-axis rotation signature close to the center.

Bendo & Barnes study the shape of the v/σ curve with radius for some merger remnants from 1:1 and 3:1 encounters. They compare it with observational data from Rix et al. (1999) and find a reasonably good agreement. However, Cretton et al. (2001) find that both Bendo & Barnes' models and their own are not able to match observations (see their figure 6). We present the same plot in figure 6.20. There we plot $V(R)/\sigma(R)$ vs. R/R_e for each model, where R is the projected radius. These plots are produced for a point of view parallel to the y-axis. This choice might seem somewhat arbitrary but it is a compromise between the symmetric point of view taken by Bendo & Barnes along the intermediate axis of symmetry of their ellipsoids and a randomly chosen point of view. Comparing this with figure 6 in Cretton et al. (2001) we see that for bulgeless systems and for equal mass mergers of bulge dominated systems the claims by Cretton et al. hold. However when we look at mass ratios 2:1 and 3:1 our systems do seem to lie closer to the data than their models. This, again may be related to the large bulge in our simulations relative to the Bendo & Barnes and Cretton et al. models.

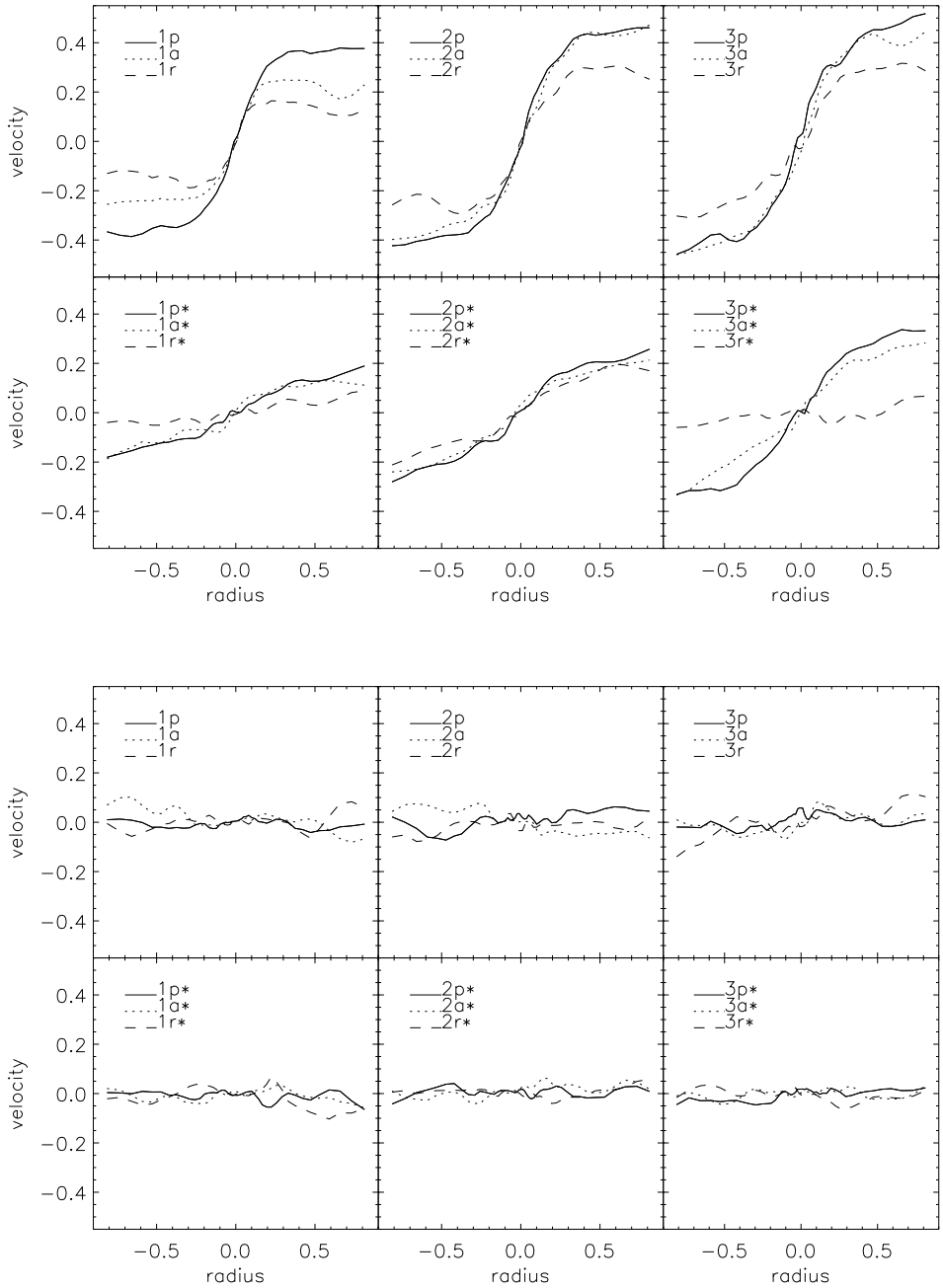

Figure 6.18— From top to bottom, the first set of panels show the rotation curve as measured along the major axis. The simulations are identified in the upper left corner. The point of view is along the y-axis. The second set of panels show the rotation curve along the minor axis from the same point of view. The top rows are models with bulge, bottom ones are bulgeless models. In each frame the mass ratio has a fixed value.

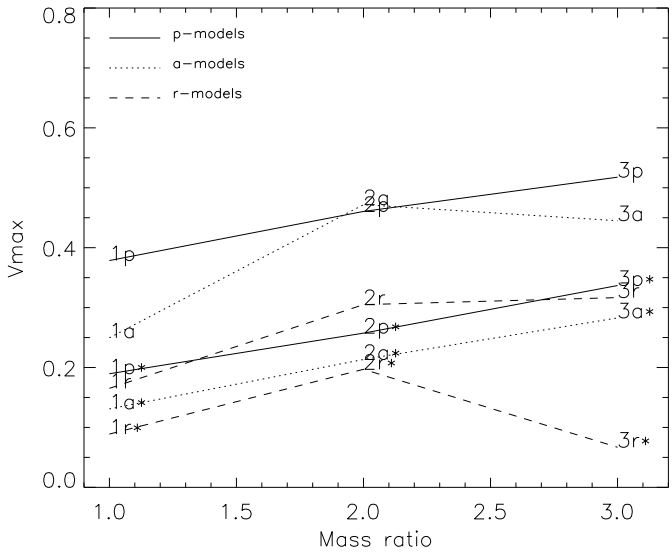

Figure 6.19— Maximum rotation velocity, V_{max}, vs. mass ratio.

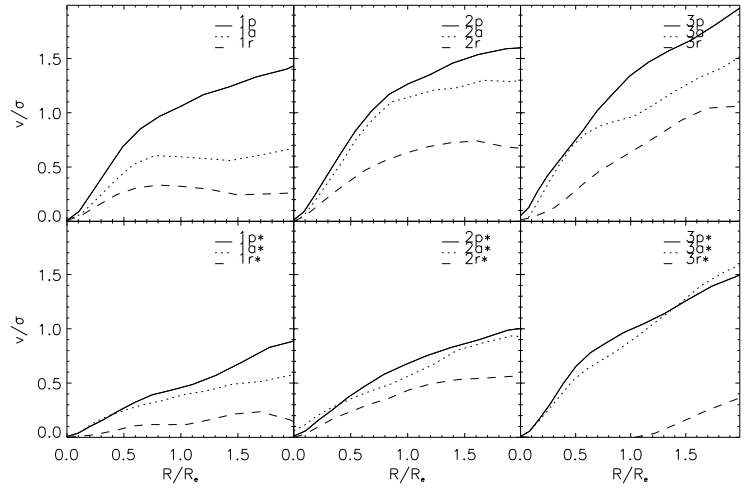

Figure 6.20— v/σ vs. radius, in effective radii. Notation as in figure 6.18. Comparison of these figures with Cretton et al. (2001) figure 6 shows that non-equal mass mergers resulting from dbh models come close to the observational values in Rix et al. (1999).

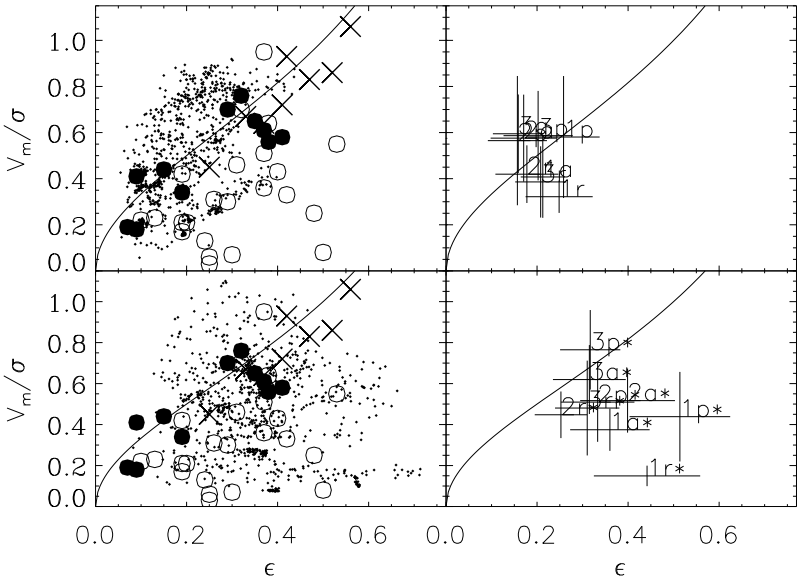

Figure 6.21— Following Davies et al. (1983) and a similar diagram in Chapter 2 of this thesis we plot here the rotation, expressed as V_m/σ_o vs. the projected ellipticity. We have measured these observables for one hundred points of view for each model. These are plotted as small dots in the left panels. A mean for each model is found and is plotted with the model name in the right panels. They are compared with data from Davies et al. (1983). Open circles are bright ellipticals, filled circles are low luminosity ellipticals and crosses are bulges. The top panels show models with bulge. These are close to the line of oblate rotators. The bottom panels show bulgeless models. These show higher flattening and they are less rotationally supported.

Rotation support vs pressure support

Whether ellipsoids owe their flattening to rotation or to anisotropy of the velocity dispersion tensor can be studied with the V_{max}/σ_o vs ϵ diagram. Binney (1978) shows that in the absence of velocity anisotropy oblate ellipsoids rotate fast (are rotationally supported) while prolate ellipsoids rotate slower. In this diagram, giant elliptical galaxies fall well below the oblate line (solid line in figure 6.21), indicating that they are mainly supported by velocity dispersion (Illingworth, 1977), while low-luminosity ellipticals scatter along the oblate line (Davies et al. 1983) indicating that their ellipticities are consistent with the galaxies being flattened by rotation. Bulges of giant spirals also scatter along the oblate line (Kormendy & Illingworth 1982, 1983). Here we investigate whether the ellipticies and rotation in the elliptical models resulting from our merger experiments fall along the oblate line or below it.

We have calculated the isophotes from a smooth binned projected particle distribution. To these isophotes we fit ellipses to obtain the ellipticity. The mean ellipticities of the isophotes have been calculated from 100 random points of view. For each of those points of view we place a slit along the major axis of the isophotes. This slit has a lenght of at least $10R_e$ so that we sample most of the system and we ensure that we include the maximum of

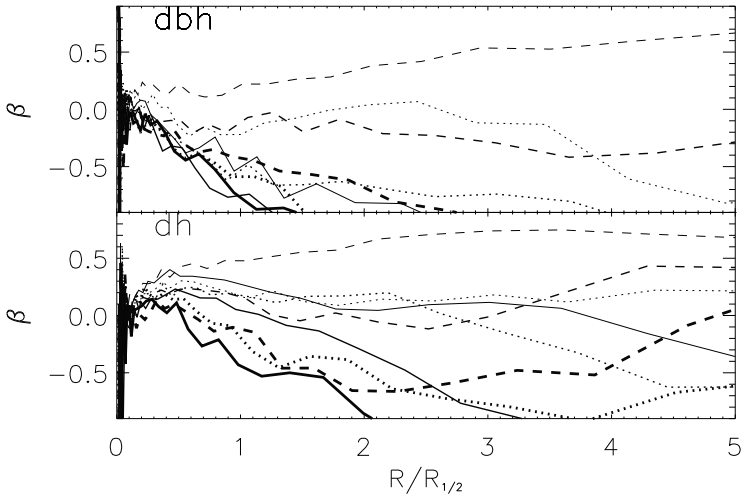

Figure 6.22— Anisotropy profiles, β vs. radius. Top panel dbh models, bottom panel dh models. 'p' models are depicted with solid lines, 'a' models are shown as dotted lines and 'r' models dashed lines. The thickness of the lines gives the mass ratio, the thinnest lines are for 1:1 mass ratios and the thickest for 3:1.

the rotation curve, V_{max}. Then, we calculate V_{max} and the central velocity dispersion, σ_o. From this we obtain the V_m/σ_o vs. ϵ diagram. A similar approach has been taken in Chapter 2, section 3.3.

The results are shown in figure 6.21. In this plot, dots represent the values for all models and for each point of view. A mean of the cloud of dots for each model has been calculated and is plotted as a number and a letter, as given before. The solid lines indicate the r.m.s. scatter for each cloud.

The models cover most of the space covered by real ellipticals, although a bigger concentration is seen close to the solid curve, mainly for heavy-bulge models. This curve represents the locus of the oblate systems supported by rotation with an isotropic distribution of residual velocities (Binney 1978).

The mean points for bulge dominated models lie close to the isotropic oblate rotator line. Bulgeless models show a trend where models from equal mass mergers are close to highly flattened non-rotating (pressure supported) systems, while when increasing the mass ratio of the initial systems, the final models are closer to the oblate line.

Anisotropy

Following the scheme of section 3.7 in chapter 2 we have calculated the anisotropy parameter as a function of radius for our models. This quantity is defined as:

$$\beta = 1 - \frac{\sigma_t^2}{2\sigma_r^2}, \tag{6.15}$$

where σ_r is the radial and σ_t the tangential velocity dispersion:

$$\sigma_t^2 = \sigma_\theta^2 + \sigma_\phi^2. \tag{6.16}$$

Here radial anisotropy means $\beta > 0$, while $\beta < 0$ means tangential anisotropy.

Profiles of β vs. radius are shown in figure 6.22. The top panel shows the dbh models, while dh models are shown in the bottom panel.

Figure 6.22 shows that the vast majority of the remnants of disk galaxies present tangentially anisotropic kinematics. In dbh mergers the remnants show tangential anisotropy well inside the half-mass radius and at large radii. Only few of these models are consistent with being isotropic, and one shows radial anisotropy. Looking into the details we find that prograde models (solid lines) are all tangentially anisotropic, anti-parallel models are tangentially anisotropic but the equal mass merger of this type is consistent with being an isotropic spheroid. The only model that shows radial anisotropy is $1r$, all other retrograde models are tangenitally anisotropic although we find a gradient with mass ratio.

Remnants of dh models show more diversity of their anisotropy characteristics. All models show some degree of radial anisotropy inside the half mass radius of the merger remnant. This is probably related to bar formation during the merging stages, as mentioned before. For the outer parts ($R/R_{1/2} > 1$) there is a variety of results but it appears that the mass ratio of the progenitors and the initial geometry play a role. For the 3:1 mass merger remnants systems show mainly tangential anisotropy, but not as prominent as in bulge dominated systems. Merger remnants from 2:1 progenitors are compatible with being isotropic. This is also true for equal mass mergers with prograde and anti-parallel orbits. It is again for the equal mass merger on a retrograde orbit that we find a radially anisotropic remnant.

The differences between dbh and dh models are mainly due to the difference in behaviour during the final merging stages. Bulgeless models are prone to bar formation, this carries angular momentum outward and leaves particles in the inner parts on mostly radial orbits, developing a radial anisotropy. In bulge dominated galaxies this is not the case since the presence of the bulge stabilizes the systems against bar formation. For equal-mass mergers the orbital configuration plays a role in determining the final state of the system. However, for non-equal mass mergers the initial configuration inside the larger disk seems to be the dominant mechanism for the presence of the tangential anisotropy. It is therefore a special combination of the initial tangential distribution (disks) and the nearly circular orbits (e=0.7) that causes our systems to show a strong tangential anisotropy.

5 Discussion

We have carried out 18 simulations of mergers between disk galaxies. These simulations are divided into two groups. The first set involves systems with a disk, bulge and a halo. The second set involves systems with disk and halo only. We have done these simulations for three different mass ratios of the progenitor systems and for three different orbital configurations, keeping the orbits for the 18 runs the same. This is by no means a complete survey but we hope it can shed some light on important questions. Similar studies by

Barnes (1992), Hernquist (1992), Hernquist (1993), Hernquist et al. (1993a), Hernquist et al. (1993b), Heyl et al. (1994), Heyl et al. (1995), Heyl et al. (1996) involve identical galaxies with several orbital configurations, but they do not take into account the possible effect of different mass ratios on the final merged system. Barnes (1998), Balcells & González (1998), Naab, Burkert & Hernquist (1999), Bendo & Barnes (2000), Cretton et al. (2001) and Naab & Burkert (2001) do explore mergers between progenitors with mass ratios from 1:1 to 3:1 including a bulge. In that sense bulgeless non-equal mass mergers are still not fully explored yet and they represent a new contribution. Another new point in the present study is that we also consider mergers of bulge systems with a bulge-to-disk ratio of 1:2. Earlier work is restricted to smaller bulge to disk ratio's of 1:3.

We find that the prominence of the tidal tails depends on the spin configuration. Symmetric tails are formed in equal mass prograde mergers. This is in perfect agreement with previous results from Toomre & Toomre (1972) and Barnes (1992). For non-equal mass mergers we find that the less massive system is the one that responds more strongly to the tidal encounter. This is true even for retrograde experiments, in which the disk spin of the less massive galaxy is anti-parallel to the orbital angular momentum. A large fraction of particles are expelled into tidal tails at the first encounters as already found by Barnes (1992). Particles closer to the center of the remnant fall back more rapidly than those further away into the tail (See Barnes 1992, Hibbard & Mihos 1995). Details of the tail formation seem therefore related to the spin-orbit coupling, but the mass ratio also plays a role. Anti-parallel and retrograde systems show different behaviour in the tidal tails. In our anti-parallel systems the largest component has its original spin coupled with the orbit while the smallest system has its spin anti-parallel to the orbit. The response of the smallest galaxy is stronger as seen from the tails that are still present after the merger is complete. For bulgeless equal mass mergers we find that tidal tails are formed during the interaction stages but the final relaxed system does not show any prominent tidal tail. This is unexpected according to what Hernquist (1992) finds. Prehaps it is related to bar formation during the first pericenter passage, this 'dissipates' some of the rotation effectively. Hernquist & Weinberg (1992) show that the interaction between the bar and a spheroidal component (the halo in this case) can drive the angular momentum away from the center into the dark halo. This could be the cause of the short tails for bulgeless simulations. The effect may be increased even further in comparison with dbh models since bulgeless systems have a higher amount of material in the halo, both enhancing the bar-halo interaction and preventing the formation of prominent tails. This bar formation occurs also in the models done by Hernquist (1992), however some of his initial configurations are too symmetric creating a maximal spin-orbit coupling, leading to the formation of more prominent tails than we find here.

When the mass ratio is different from one the final morphology of merger remnants in bulgeless systems also depends strongly on the initial spin configuration. While parallel-configurations do show a prominent tail, this time due to the asymmetric response to the tidal field introduced by the mass difference between the progenitors, anti-parallel and retrograde configurations appear to show shell formation in the final stages.

Dubinski et al. 1996, Mihos et al. 1998 and Dubinski et al. 1999 try to use the tidal tails to constrain the mass and the depth of the potential well of the dark matter halo around disk galaxies. However Barnes (1998) finds that long tails would constrain the potential well depth but not the halo mass and that the results of the previous authors are model dependent.

When comparing this set of disk encounters with those presented in previous chapters between spheroids we find that tidal tails are more conspicuous for disk models.

Hernquist & Quinn (1988) and Hernquist & Spergel (1992) study the formation of shells

in mergers. Hernquist & Spergel (1992) show that through major mergers of bulgeless disk systems (mass ratio 1:1) it is in fact possible to form shells via phase wrapping. This is achieved when the material in the tidal tails returns to the relaxed central body, leaving the characteristic shell structure. They find that prograde orbits result in the formation of shells. The shells in their remnants are aligned with the major axis of the final system, although their orbits are highly symmetric, with a perfect alignment of the disks. The spin-orbit coupling is maximized in some of their configurations and may give results that would not appear in a less symmetric set-up.

We find as well that the geometry of the orbit influences the final configuration of the shells. The material in the tails is bound and will fall back to the inner potential well. An observational example may be NGC 3656, see Balcells et al. (2001). It could be happening already in our simulations but due to the lack in resolution (low number of particles) we might miss it. However, this process could be strongly dependent on the size of the bulge. For bulgeless non-equal mass mergers we find a distinct signature of the presence of shells even though our particle resolution is rather low. Here the dynamical mechanism is the same as that in minor mergers, i.e. phase wrapping as explained by Hernquist & Spergel (1992).

Merrifield & Kuijken (1998) use the sharp features presented by shells in the V_r vs. R diagram, when measured projected along a slit, to determine the potential well of elliptical galaxies. We find sharp features in the V_r vs. R diagram. We note that when plotting V_r and V_t vs. the energy there are also coherent groups of particles with the same energy and a range of radial velocities. Same energy means same R_{apo}, as created by a shell through phase wrapping. The bands are sightly oblique, i.e. with less bound material for $V_r > 0$. These bands seem to correlate with those seen in the V_t diagram. This might indicate that the particles on those bands are not on perfectly radial orbits.

Our models show that, while the inner parts are close to triaxial, when going outwards they become more oblate. This was already found for equal mass mergers of bulge disk by Barnes (1992). In that paper, Barnes explores equal mass mergers and finds that the initial orbital parameters determine where the system will end in the triaxiality diagram. For those of his models similar to ours (2-3-5) the values of the axis ratios are comparable. For non-equal mass mergers on the other hand we find larger values for the axis ratios, in other words the systems are more spherical.

Our dbh models show that 1:1 mergers are more triaxial than non-equal mass mergers, which are oblate. This is a result of the stronger tidal friction in equal-mass mergers which leads to more nearly radial orbits near the end of the merger process. A difference however arises between systems with a bulge and bulgeless systems. Systems with bulge end up nearly oblate while bulge-less systems end up triaxial. This may be due to the fact that bulgeless models are more prone to bar distortion during orbital decay due to the tidal field. Also the fact that our initial bulge-disk systems are bulge dominated, with massive bulges, could cause our final remnants to be much rounder than those by Barnes (1998) and Hernquist et al. (1995).

Hernquist (1993) finds his bulgeless systems to behave differently than those explored by Barnes (1992). Our dh systems, specially 1:1 mergers, show lower axis ratios than dbh. The presence of a bulge is therefore key in the shape the remnant is ultimately going to have. The spin configuration is also crucial as argued above.

We find a discrepancy with previous work regarding axis ratios. Barnes (1998) finds, for mergers of two Sb-like disk galaxies, that non-equal mass mergers yield more flattened systems than the equal-mass mergers. We find the opposite. This can be due to the different initial configurations. While Barnes is merging two Sb's (disk-to-bulge mass ratio of 3:1) we

do mergers of Sa's (disk-to-bulge 2:1). Although it may seem that this is not a big difference, the material in the bulge for these mergers ends up in the inner parts of the remnant. For bulge dominated systems the massive bulge will end up in the inner parts of the remnant together with the bulge of the smaller system and they account for a large fraction of the particles at small radii (up to 60% of the luminous mass inside the half-mass radius). Accordingly, one would expect the system to become more flattened at larger radii and this is the case. These bulges are initially flattened and after the mergering they are slightly rounder. Comparing with the results from previous chapters we find a trend in the amount of mass the system should have initially in a spheroidal component in order to fully cover the axis-ratio plane given by Franx et al. (1991).

The surface density profiles of our merger models can be well fitted by a de Vaucouleurs profile. In this sense they all can be regarded as elliptical galaxies, in agreement with previous work (Barnes 1992, Hernquist 1992, 1993). We have done a fit of the surface density profile to a $r^{1/n}$ Sersic law (1968) as well. For dbh models we find that the initial spin configuration affects the final exponent n. Parallel orbits yield higher exponents for the same mass ratios. There is also a weak trend with mass ratio: encounters between galaxies of equal mass produce higher n. For non-equal mass systems the larger galaxy is not completely destroyed and therefore in the outer parts there are some hints that the original disk are still present. Such systems, similar to S0 galaxies, should be fitted with a combined Sersic plus exponential law, as done by e.g. Aguirre, Balcells & Peletier (2001).

For remnants of dh models, Sersic fits to the surface brightness profiles yield lower values of n than in dbh remnants. This difference might be due to their lower central densities due to the absence of a bulge in the precursor galaxies.

For all merger remnants the profiles deviate from both the de Vaucouleur and the Sersic law at large radii. This may be due to a combination of two processes. Some material might still not be fully virialized at these radii and might still be falling down to the inner parts. All systems were let to relax after merging for about 10 time units (this is of the order of 40 half-light crossing times). The profiles seem to depart from a good fit by either Sersic or de Vaucouleurs profiles around a radius of 3 units. This radius includes about 95% of the luminous mass in our models. The dynamical crossing time there is around 10 time units. So the outermost parts have not yet completely relaxed. A second factor could be that in the outer parts the disks have not fully been destroyed.

We have studied the concentration index defined by Trujillo et al. (2001), C_{R_e}. We find a trend of C_{R_e} with the central velocity dispersion, this was also reported for real-life elliptical galaxies by Graham et al. (2001).

We find that equal mass mergers result in systems with a boxy deviation in their isophotes, while increasing the mass ratio the systems become more disky. This was already pointed out by Naab et al. (1999). Most likely the larger disk has not been fully destroyed. Bulgeless models look in general more boxy regardless of the mass ratio of the progenitors, although the radius where the system becomes disky decreases with mass ratio. This tells us that for the final system with a disky deviation a non-equal mass merger between bulge dominated systems should probably be preferred. In this sense our models differ from those of Naab & Burkert (2001). Bender et al. (1994) find a correlation between the a_4 parameter and the kinematic h_3 parameter that gives the skewness of the line of sight velocidy distribution. Naab & Burkert (2001) find that their models for disky elliptical galaxies coming from 3:1 mergers of disks are not able to reproduce this correlation. Our bulge dominated models (dbh) seem a good benchmark to test this and to see if they are indeed a viable model for disky low luminosity ellipticals. This remains still to be done.

Boxiness-diskiness has been claimed to be point of view dependent (Fasano 1991, Sti-

avelli et al. 1991, Ryden 1992, Governato et al. 1993, Heyl et al. 1994, this thesis chapter 2). We find that this is also true for our disk-disk mergers. A system can be seen as either boxy or disky depending on the point of view.

Merger remnants originating from dbh models have higher rotation speed than those produced by bulgeless systems, as found by Hernquist (1993) and Heyl et al. (1996). When the amount of rotation is compared with the ellipticity we find that dbh models do keep a high amount of rotation while being fairly round ($\epsilon = 0.2$). In the V_{max}/σ_o vs. ϵ plot the spin configuration also plays a role. Parallel orbits leave behind a rotationally supported system rather than a pressure supported one. The mass ratio also plays a role since equal mass mergers are less rotationally supported than non-equal mass mergers, this is in agreement with Naab et al. (1999). This is mainly due to the fact that the final rotation curve depends on the mass of the larger initial system.

For mergers with the same initial mass ratio we find a range of amplitudes of the rotation curve. The spin-orbit coupling depends on the orbital configuration, and this determines whether the final systems retains a memory of the initial rotation. This was pointed out by Bendo & Barnes (2000).

For bulgeless systems we find weaker rotation. Bar formation is more likely in those systems (Hernquist 1992), and the bar transfers part of the angular momentum to the outer parts (halo) of the system, leaving the inner parts almost without trace of rotation.

Weak minor-axis rotation in the inner parts of some configurations may be due to a misalignment of the merger orbit with respect to the major axis of the larger galaxy as pointed out by Bendo & Barnes (2000).

We find that the presence of a bulge determines, not only the central density of the final merged system, as stated previously by Hernquist (1993), but may also present a solution for a number of problems. For instance, let us take the case of low luminosity elliptical galaxies. Barnes (1998) proposes 3:1 mergers as a possible formation scenario for this type of ellipticals. However, Cretton et al. (2001) argue that collisionless simulations of disk galaxies cannot account for the high amount of rotation seen in low-luminosity elliptical galaxies. A solution to this problem may be provided by the presence of a significant bulge. Cretton et al. use as initial models disk galaxies with a disk-to-bulge ratio of 3:1. We argue here that models without bulge are not able to reproduce the data by Rix et al. (1999) abouth the variation with radius of $v(r)/\sigma$. However 3:1 mergers of disk galaxies with disk-to-bulge ratio of 2:1 can account for the steep rise in the inner parts they observe for these low-luminosity elliptical galaxies. Therefore we propose a merging scenario for this type of elliptical galaxies via 3:1 mergers involving heavy-bulge galaxies.

Bulgeless systems show less rotation than bulge systems. The initial orbits are not energetic enough to decrease the ellipticity beyond certain limits. Systems are now flatter ($\epsilon \sim 0.4$). Here also the mass ratio is the dominant parameter: mass ratios of order 3:1 give systems that are more nearly rotationally-supported than equal-mass mergers, with spin orientation playing a secondary role.

Given all these detailed characteristics the 'merger hypothesis' as formulated by Toomre & Toomre (1972) clearly is a plausible formation scenario for elliptical galaxies. Equal-mass mergers give, depending on the initial configuration, slowly rotating, mostly boxy, pressure supported systems, quite similar to normal elliptical galaxies. Nieto & Bender (1989) give a phenomenological classification for boxy elliptical galaxies depending on the amount of rotation. 1:1 mergers could describe types I and II in their scheme. Non-equal mass mergers end in rapidly rotating, mostly disky systems, and, depending on the amount of bulge mass involved, they could be the progenitors for low-luminosity elliptical galaxies, contrary

to what Cretton et al. (2001) state. Furthermore, merger remnants of these encounters are likely to experience more mergers, with results highlighted in chapters 2 and 4 of this thesis.

On the whole, the merger hypothesis can be viewed in a simple and naive way as follows. In a distant past, gas-dominated disk galaxies may gain their bulges via accretion of smaller galaxies (see Aguerri et al. 2001). This accretion consumes part of the gas of the galaxy. As the disk galaxies accrete more and more satellites the bulge of the system grows and the gas content of the galaxy decreases. This mechanism can be enhanced due to ram-pressure stripping. Major mergers between gas-rich disks are likely to happen as well. The result would be an elliptical galaxy with a young population of stars at its center due to a massive starburst during the merger stages, consuming most of the gas. This can yield as a result low-luminosity disky E's. However, non-equal mass mergers of heavy-bulge gas free disk galaxies (Sa type) can give very similar results, resulting in a spread of characteristics of these galaxies.

Equal mass mergers of Sa's can also give as a result medium-luminosity elliptical galaxies. High-luminosity elliptical galaxies may come from subsequent mergers of the spheroids previously formed. Elliptical galaxies then can be viewed as the result of the merger process but not as the final step since mergers between E's are likely to happen in the course of time.

Bibliography

Aguerri, J. A. L., Balcells, M. & Peletier, R. F., 2001, A&A, 367, 428.

Balcells, M., & Gonzalez, A. C., 1998, ApJ, 505, L109.

Balcells, M., van Gorkom, J. H., Sancisi, R. & del Burgo, C., 2001, AJ, 122, 350.

Barnes, J. E., 1988, ApJ, 331, 699.

Barnes, J. E., 1992, ApJ, 393, 484.

Barnes, J. E., 1998, astro-ph/9811091

Barnes J.E. & Hernquist L.,1992 ARA&A, 30, 705

Bekki, K., 1998, ApJ, 496, 713.

Bender, R., Saglia, R. P. & Gerhard, O. E., 1994, MNRAS, 269, 785.

Bendo, G. & Barnes J.E., 2000, 319, 315.

Binney, J., 1978, MNRAS, 183, 501.

Binney, J. & Merrifield, M., 'Galactic Astronomy', 1998, Princeton University Press.

Capelato, H. V., de Carvalho, R. R. & Carlberg, R. G., 1995, ApJ, 451, 525.

Cretton, N., Naab, T., Rix, H.-W. & Burkert, A., 2001, ApJ, 554, 291.

de Vaucoleurs, G., 1958, Handbuch der Physik, 53, 311.

de Zeeuw, T. & Franx, M., 1991, ARA&A, 29, 239.

Davies, R. L., Efstathiou, G., Fall, S. M., Illinworth, G., & Schechter, P. L. 1983, ApJ,266,41.

Dubinski, J., Mihos, J C. & Hernquist, L., 1996, ApJ, 462, 576.

Dubinski, J., Mihos, J C. & Hernquist, L., 1999, ApJ, 526, 607.

Fasano, G., 1991, MNRAS, 249, 208.

Fish, R. A., 1964, ApJ, 139, 284.

Franx, M., Illingworth, G., & de Zeeuw, T., 1991, ApJ, 383, 112.

Gerhard, O. E., 1983, MNRAS, 202, 1159.

Governato, F., Reduzzi, L. & Rampazzo, R., 1993, MNRAS, 261, 379.

Graham, A. W., Trujillo, I. & Caon, N., 2001, AJ, 122, 1707.

Hernquist, L. 1990, J. Comp. Phys., 87, 137.

Hernquist, L. 1992, ApJ, 400, 460.

Hernquist, L. 1993, ApJ, 409, 548.

Hernquist, L. & Barnes, J. E., 1991, Nature, 354, 210.

Hernquist, L. & Quinn, P. J.,1988, ApJ, 331, 682.

Hernquist, L. & Spergel, D. N., 1992, ApJ, 399, L117.

Hernquist, L. & Weinberg, M. D., 1992, ApJ, 400, 80.

Hernquist, L., Spergel, D. N. & Heyl, J. S., 1993, ApJ, 416, 415.

Heyl, J. S., Hernquist, L. & Spergel, D. N., 1994, ApJ, 427, 165.

Heyl, J. S., Hernquist, L. & Spergel, D. N., 1995, ApJ, 448, 64.

Heyl, J. S., Hernquist, L. & Spergel, D. N., 1996, ApJ, 463, 69.

Hibbard, J. E. & Mihos, J. C., 1995, AJ, 110, 140.

Illingworth, G. 1977, ApJL, 218, L43

King, I. R., 1966, AJ, 71, 64.

Kormendy, J. & Illingworth, G., 1982, ApJ, 256, 460.

Kormendy, J. & Illingworth, G., 1983, ApJ, 265, 632.

Kuijken, K., Dubinski, J., 1994, MNRAS, 269, 13.

Kuijken, K., Dubinski, J., 1995, MNRAS, 277, 1341

Merrifield, M. F. & Kuijken, K., 1998, MNRAS, 297, 1292.

Mihos, J. C., Dubinski, J. & Hernquist, L., 1998, ApJ, 494, 183.

Naab, T., Burkert, A. & Hernquist, L., 1999, ApJ, 523, L133.

Naab, T. & Burkert, A., 2001, ApJ, 555, L91.

Nieto, J.-L. & Bender, R., 1989, A&A, 215, 266.

Ostriker J.P., 1980, Com Ap, 8, 177.

Prieur, J. L., 1990, in *Dynamics and Interactions of Galaxies*. ed. R. Wielen, (Berlin: Springer-Verlag), 72.

Rix, H.-W., Carollo, C. M. & Freeman, K. C., 1999, ApJ, 513, L25.

Ryden, B. S., 1992, ApJ, 386, 42.

Sakai, S., Mould, J. R., Hughes, S. M. G., et al. , 2000, ApJ, 529, 698.

Schweizer, F., 1998, in 'Galaxies: Interactions and Induced Star Formation', Saa-Fee Advanced Course 26. Springer-Verlag. Eds. Friedli, D., Martinet, L. and Pfenniger, D.

Sersic, J.-L., 1968, 'Atlas de Galaxias Australes, (Cordoba: Obs. Astrnómico).

Shu, F. H., 1969, ApJ, 158, 505.

Stiavelli, M., Londrillo, P. & Messina A., 1991, MNRAS, 251, 57.

Toomre, A., 1977, in 'The evolution of Galaxies and Stellar Populations', Ed. Tinsley, B. & Larson, R.

Toomre, A.& Toomre, J., 1972, ApJ, 178, 623.

Trujillo, I., Graham, A. W. & Caon, N., 2001, MNRAS, 326, 869.

Ziegler, B. L., Bohm, A., Fricke, K. J., Jager, K., Nicklas, H., Bender, R., Drory, N., Gabasch, A., Saglia, R. P., Seitz, S., Heidt, J., Mehlert, D., Mllenhoff, C., Noll, S., Sutorius, E., 2002, ApJ, 564, 69.